PLASMA DYNAMICS

XI. PLASMA PHYSICS*

Academic and Research Staff

Prof. S. C. Brown	Prof. G. Bekefi	J. J. McCarthy
Prof. W. P. Allis	Prof. J. C. Ingraham	W. J. Mulligan

Graduate Students

M. L. Andrews	V. G. Forrester, Jr.	G. L. Rogoff
A. J. Cohen	E. V. George	J. K. Silk
D. L. Flannery	P. W. Jameson	D. W. Swain
	R. L. Kronquist	J. H. Vellenga

A. COMPUTER PROGRAMMED "BASIC DATA OF PLASMA PHYSICS"

As mentioned in Quarterly Progress Report No. 80,[1] an attempt has been made to revise the 1959 edition of "Basic Data of Plasma Physics" (Special Technical Report Number 2 of the Research Laboratory of Electronics, M. I. T., published by The Technology Press, Cambridge, Mass., and John Wiley and Sons, Inc., New York) by using the information retrieval service of the Library TIP Program. Details of the operation of this experiment have been published,[2] and therefore will not be outlined again here.

This step in the project has now been completed with the publication of the book Basic Data of Plasma Physics, 1966.[3] The production of this volume was accomplished completely from a remote compatible time-sharing system console, and therefore, in principle, could have been done at any distance from the computer connected (as it was) by an ordinary telephone line. To simulate a completely remote access endeavor, we avoided going to the library in the process of collecting these data. When a relevant reference appeared on the teletype output, we checked the teletype record and mailed it to the library, and the library returned to us a Xerox copy of the paper. The overall average of extra material that was thus delivered came out to be approximately 10 per cent; that is, 90 per cent of the called-for Xerox copies of the entire paper were actually used. Drawings of the data were then made to be included in the book as illustrations, and the references are shown in standard TIP nomenclature, so that the material in the book may be updated by further use of the citation technique inherent in information retrieval from the TIP library.

It should be emphasized that this information retrieval system completely by-passes the standard abstracting. One goes directly from title and bibliography search to the paper itself. The abstract is not a useful step in this procedure.

The index was also prepared with the aid of an IBM 7094 computer, the program for doing this being at the M. I. T. Computation Center. Items indexed are subject and author reference, which consists of one word or more. The computer produces a list

---

*This work was supported by the United States Atomic Energy Commission under Contract AT(30-1)-1842.

of cyclic permutations of each reference, successive permutations being with the different words of four or more letters appearing in the reference. Words originally to the left of the "key word" appear at the right end of the line, while the page number of the reference is placed to the left of the line. After forming permutations of all entries, the computer alphabetizes them according to the key word. Permutations of multiple-author listings follow the same form. Because the index is a reproduction of the computer printout, subscripts and superscripts are not used. Thus H_2O appears as H2O. The number of charge units on an ion is indicated by an equal number of plus or minus signs following the chemical symbol for the atom or molecule. The index is unusually complete and consists of an author index, a subject index, and an index of chemicals.

S. C. Brown

References

1. S. C. Brown, "Computer Programmed 'Basic Data of Plasma Physics,'" Quarterly Progress Report No. 80, Research Laboratory of Electronics, M. I. T., January 15, 1966, pp. 83-85.
2. S. C. Brown, Physics Today 19, 59-64 (May 1966).
3. S. C. Brown, Basic Data of Plasma Physics, 1966 (The M. I. T. Press, Cambridge, Mass., 2d edition (revised), 1967).

B. FAR INFRARED PLASMA DIAGNOSTICS

1. Introduction – Quantities Measured

A wide-bandwidth Michelson interferometer has been used to measure phase shifts caused by a repetitively pulsed plasma over the spectral range from $k = 1/\lambda = 8\text{-}55\ \text{mc}^{-1}$. Line densities NL (where N is the electron density, and L the length of the plasma) in the vicinity of 3×10^{14} electrons cm^{-2} have been measured with an accuracy of a few per cent.

The observed phase shift, $\Delta\phi$, is given by

$$\Delta\phi(\omega) = \frac{\omega}{c}\int_0^{2L} |1 - \text{Re}\,\mu(x,\omega)|\,dx \text{ radians,} \tag{1}$$

where $\mu(x,\omega)$ is the complex refractive index of the plasma at a frequency ω. It is given by[1]

$$\mu^2 = 1 - \left(\frac{\omega_p}{\omega}\right)^2 \left[\frac{1}{1+\left(\frac{\nu}{\omega}\right)^2} + \frac{j\frac{\nu}{\omega}}{1+\left(\frac{\nu}{\omega}\right)^2}\right]$$

and approximated, in the limits $\left(\frac{\nu}{\omega}\right)^2 \ll 1$ and $\left(\frac{\omega_p}{\omega}\right)^4 \ll 1$, by

$$\mu = 1 - \frac{1}{2}\left(\frac{\omega_p}{\omega}\right)^2 - j\left[\frac{1}{2}\frac{\nu}{\omega}\cdot\left(\frac{\omega_p}{\omega}\right)^2\right],$$

where ν is the electron collision frequency for momentum transfer,[2] and ω_p the plasma frequency.

In this approximation the phase shift is given by

$$\Delta\phi(\omega) = \frac{1}{2\omega c}\int_0^{2L} \omega_p^2(x)\,dx$$

$$= \frac{(5.65\times10^4)^2}{2\omega c}\int_0^{2L} N(x)\,dx$$

$$= \frac{5.32\times10^{-2}}{\omega} <N>\,2L \text{ radians}$$

$$\therefore \quad <N> = \frac{\omega}{5.32\times10^{-2}\times 2L}\,\Delta\phi(\omega)\ \text{cm}^{-3}.$$

In connection with the present experiment, it is convenient to express ω in terms of the free-space number $k = 1/\lambda\ \text{cm}^{-1}$.

Thus the average electron density is given by

$$<N> = \frac{2\pi c k}{5.32 \times 10^{-2} \times 2L}$$

$$= \frac{3.54 \times 10^{12}}{2L}\, k\Delta\phi(k)\ \text{cm}^{-3}. \tag{2}$$

In the present case, 2L = 15 cm

$$\therefore \quad <N> = 2.36 \times 10^{11}\, k\Delta\phi(k)\ \text{cm}^{-3}. \tag{3}$$

As the beam traverses radially through a cylindrical discharge of radius R, the radial dependence of N is probably close to that of a zero-order Bessel function,[2] that is,

$$N(\nu) = N_o J_o\left(2.405 \frac{\nu}{R}\right),$$

where N_o is the electron density at the center of the discharge.

$$\therefore \quad <N> = \frac{N_o}{2.405} \int_0^{2.405} J_o(r)\, dr$$

$$\approx 0.6 N_o$$

$$\therefore \quad N_o \approx 1.7 <N>. \tag{4}$$

It is also convenient in the present experiment to express the density in terms of $k_{2\pi}$, the wave number at which the phase shift caused by the plasma is exactly 2π. From Eq. 3, it is found that

$$<N> = 1.48 \times 10^{12}\, k_{2\pi}. \tag{5}$$

2. Interferometric Method

It is well known that Fourier transform spectroscopy[3] is the most efficient of available methods for examining a wide spectrum when resolution is energy-limited, as is the case in the far infrared region. For this reason, it is the method used throughout the studies described here. A description of the principles involved may be found in a previous report,[5] and comprehensive discussions have been published.[3,4,6]

The interferometer used here has also been discussed in detail elsewhere.[7] It is a simple Michelson interferometer that has been demonstrated to be capable of a spectroscopic resolution, Δk, of less than 0.3 cm^{-1} when used for Fourier transform spectroscopy. The spectrum for the present experiments ranges from 8 cm^{-1} to 55 cm^{-1}.

The fundamental principle of this method is the same as that of a Rayleigh refractometer,[8] or of other far infrared refractometers used to make such phase-shift measurements.[9,10] Two mutually coherent beams of light interfere to produce a fringe pattern. Introduction of a refractive sample into one of the two beams produces a displacement of the fringe pattern which is proportional to the path difference created by the sample. In Rayleigh's case the radiation is monochromatic and the fringe shift easily observable. In the present case, the radiation is not monochromatic and, moreover, the fringe shift is a strong function of frequency and not directly observable. By comparing the Fourier transforms of the shifted and unshifted fringe patterns (interferograms), it will be shown that it is easy to find those wave numbers at which the fringe shift is an exact multiple of the half-wavelength.

Owing to the low signal-to-noise ratios found in the far infrared region, it is usually necessary to use synchronous detection to observe the infrared signal. This means that the signal observed from the lock-in amplifier is the difference between two signal levels (usually "on" and "off"). Consider the effect of chopping the infrared signal in one arm of the interferometer with a refractive medium. If the signal is detected synchronously with the chopper, the resulting signal is the <u>difference</u> between the unperturbed interferogram and the phase-shifted interferogram. If at any given frequency the phase shift is an even multiple of π, this difference signal becomes zero, and if the phase shift is an odd multiple of π, the signal attains a maximum. The location of the wave numbers at which these maxima and minima occur is equivalent to measuring discrete phase shifts at specific frequencies.

This argument can be expressed quantitatively. When a power spectrum $\mathscr{I}(k)$ passes through the interferometer, the detector signal $I_o(x)$ (where x is path difference) is given by

$$I_o(x) = \int_0^K \mathscr{I}(k) \cos\left[2\pi kx+\phi_1(k)\right] dk, \tag{6}$$

where K is a value of k above which $\mathscr{I}(k)$ is negligible, and $\phi_1(k)$ is a phase shift, of no direct physical interest, depending upon such factors as beam-splitter and mirror misalignment and, more importantly, the crystal quartz windows to the discharge tube in one of the interferometer arms.

Normally, $I_o(x)$ is Fourier transformed by digital computer to obtain

$$\mathscr{I}'(k) = \mathscr{I}(k') * \chi(k-k'), \tag{7}$$

where "*" denotes "convolved with," and $\chi(k)$ is the scanning function or linewidth that is described in section 5 of this report.

When a plasma is present in one of the two beams, the phase shift ϕ_1 becomes ϕ_2, so that

$$\Delta\phi(k) = |\phi_1(k)-\phi_2(k)|,$$

where $\Delta\phi(k)$ is the phase shift caused by the plasma, given by Eq. 2.

The difference signal thus becomes

$$I_{\text{diff}}(x) = \int_0^K \mathscr{I}(k)\,\{\cos\,[2\pi kx+\phi_1(k)] - T(k)\cos\,[2\pi kx+\phi_2(k)]\}\,dk, \tag{8}$$

where T(k) is the effective transmission coefficient of the plasma. After some algebraic manipulations, Eq. 8 becomes

$$I_{\text{diff}} = \int_0^K \mathscr{I}(k)\,R(k)\cos\,[2\pi kx+\gamma(k)]\,dk \tag{9}$$

where R(k) may be called the response function of the interferometer. It is given by

$$R(k) = \sqrt{1 + T^2(k) - 2T(k)\cos\,[\Delta\phi(k)]} \tag{10}$$

and may easily be determined from the ratio of the transforms of $I_o(x)$ and $I_{\text{diff}}(x)$. The phase term in Eq. 9 is given by

$$\gamma(k) = \frac{\sin\phi_1(k) - T(k)\sin\phi_2(k)}{\cos\phi_1(k) - T(k)\cos\phi_2(k)}$$

but it is not observed, as is explained in connection with the scanning function in this report.

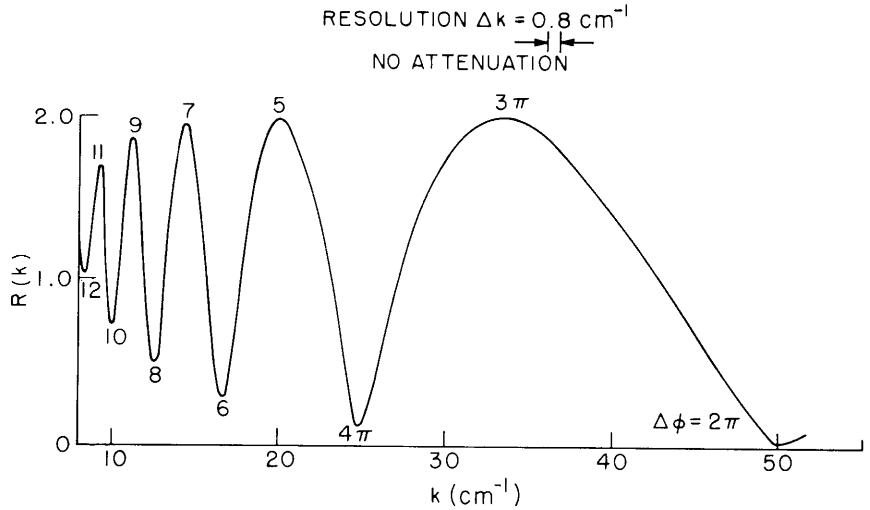

Fig. XI-1. Theoretical interferometer response for electron line density. NL = 1.11 × 10^{15} electron cm^{-2}.

It is obvious from Eq. 10 that R(k) will pass through minima when $\Delta\phi(k) = 2n\pi$ and maxima when $\Delta\phi(k) = (2n+1)\pi$ for $n = 0, 1, 2 \ldots$.

R(k) is illustrated in Fig. XI-1 for the particular case of a plasma, where $\Delta\phi(k)$ is given by Eq. 2, and of such a line density that $k_{2\pi} = 50$, that is, $\Delta\phi(50) = 2\pi$ radians. The effect of the finite instrumental linewidth (discussed below) is also taken into account in the numerical calculation for Fig. XI-1. A resolving power of 0.8 cm^{-1} was approximated by setting $\chi(k-k')$ of Eq. 7 equal to unity for $(k-k') < 0.4$ and zero elsewhere. If the instrumental linewidth were infinitely narrow, R(k) would oscillate everywhere between 0 and 2.0; Fig. XI-1 gives a more realistic expectation.

The maxima and minima of R(k) can now be located and each one can now be converted to a data point for a plot of $\Delta\phi(k)$ against k, in the manner that will be demonstrated below.

3. The Electronic System

The plasma is pulsed 30 times a second, this rate is determined chiefly by conveniently available power sources for the plasma pulse. The detector signal is sampled by a gated amplifier 60 times a second, alternately in the presence and absence of the plasma, in the manner commonly used for the examination of weak transient repetitive signals.[11] Following this standard procedure, the gate signals are fed to a pulse stretcher which converts the series of gate spikes to a square wave. The square wave, whose amplitude is proportional to the difference in height between alternate spikes, is fed to a lock-in amplifier. Figure XI-2 is a simplified block diagram of the entire system. The plasma is fired by discharging a two-stage 2-μfd delay line by means of a thyratron switch. The resulting current pulse (shaped by the delay line) is approximately rectangular, 50 μsec long, with a rise time of approximately 5 μsec and decay time of approximately 20 μsec. A peak current of 200 amps is obtainable. The trigger to the thyratron comes from the central timing unit, which in turn is locked to the 60-cps AC power line. At a variable but well-determined delay time following the plasma pulse, the gated amplifier is opened (for 3, 10, or 20 μsec) and opened again one half-cycle later. The trigger for the gated amplifier comes from the central timing unit, which also generates a 30-cps reference signal (which is always in phase with the sampling pulses, not with the thyratron triggers) for the lock-in amplifier. The central timing unit also coordinates the behavior of the pulse stretcher with that of the gated amplifier.

The data must be collected in such a way that it can easily be fed to a digital computer. The signal (voltage level) leaving the lock-in amplifier is fed to an analog-to-digital converter (in this case a digital voltmeter, DVM), thence to a digital printer. The resulting printed list of numbers is fed to the "Project MAC" time-shared computer[12] via a teletype console upon which the processed data from the computer are also displayed.

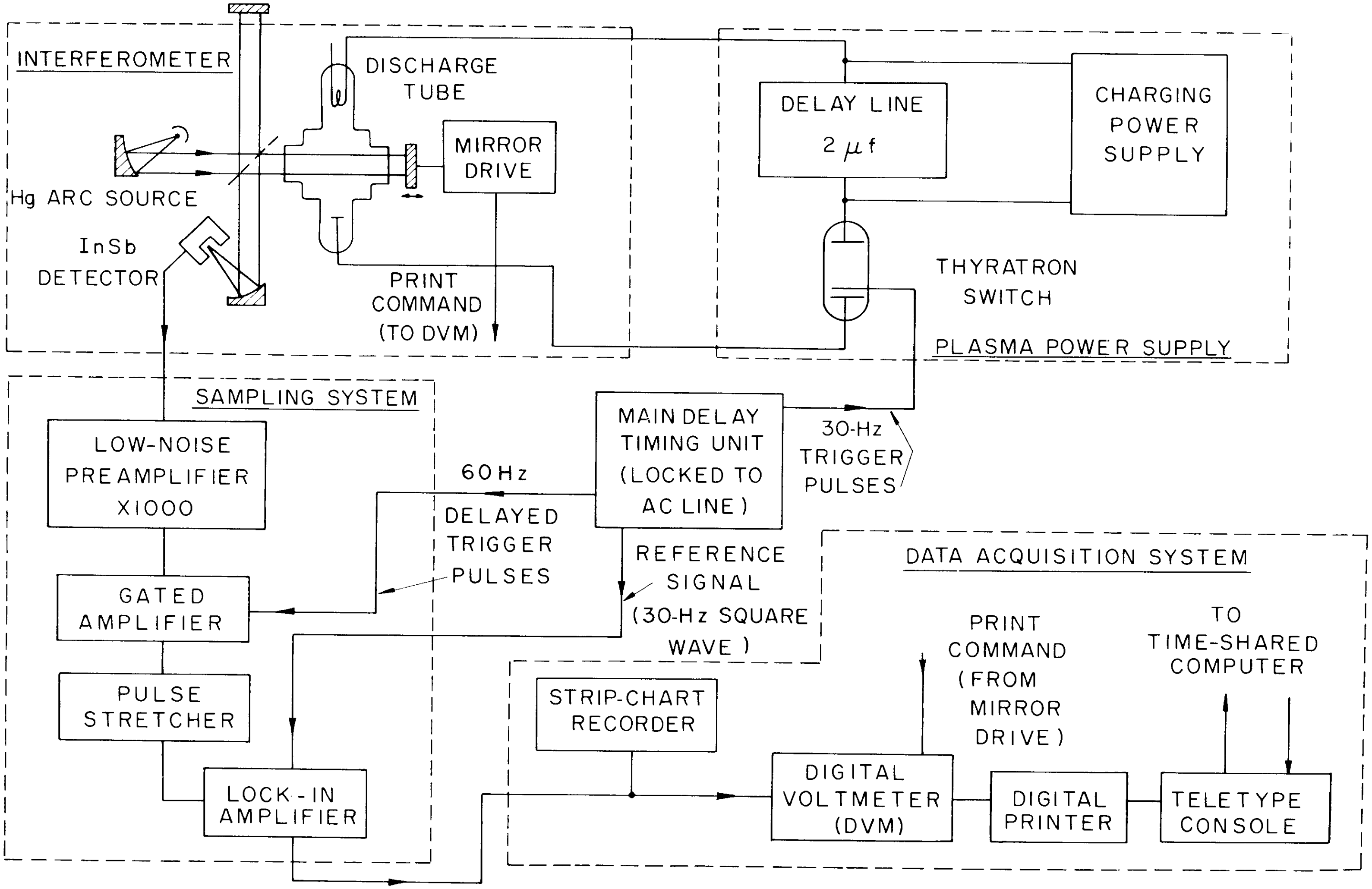

Fig. XI-2. Experimental arrangement.

Each data point represents the signal from the "lock-in" which corresponds to a given value of path difference in the interferometer. Therefore, the D. V. M. is commanded (by means of a cam in the mirror drive mechanism) to record the voltage presented to it every time the path difference has changed by 42. 3 μsec. (This sampling interval will discussed further below.)

4. Performance of the System

Initially, the method was tested by simulating the pulsed plasma with a polyethylene chopper blade, 1 mm thick, which chopped one of the interferometer beams at 30 cps.

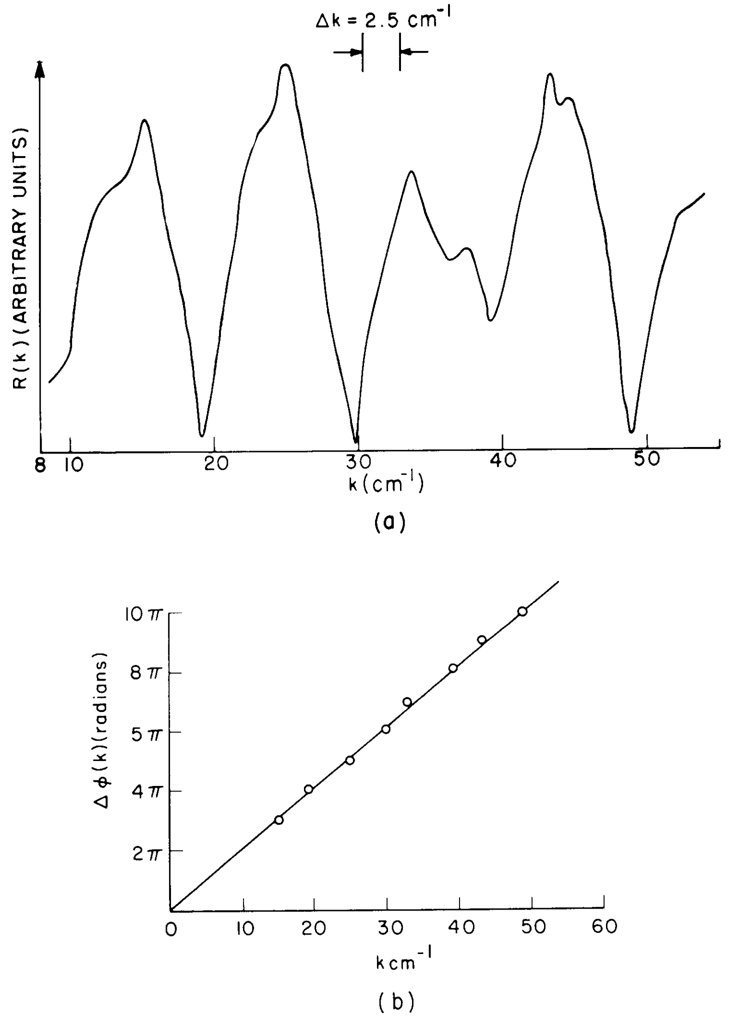

(a)

(b)

Fig. XI-3. (a) Typical interferometer response for polyethylene sample.
(b) Interpretation of (a).

Polyethylene was used because it is refractive, but not very strongly reflective, and has a fairly high transmission coefficient in this region.

The response of the interferometer, R(k), is obtained approximately by taking the ratio of the spectrum $[R(k')\mathscr{I}(k)] * \chi(k-k')$ obtained by transforming $I_{\text{diff}}(x)$ to the "normal" spectrum, $\mathscr{I}(k') * \chi(k-k')$, obtained by chopping the infrared source mechanically.

The R(k) obtained in this way is shown in Fig. XI-3a. The expected maxima and minima are easily seen. With the a priori knowledge that the refractive index of polyethylene is a weak function of k, it is to be expected that the phase shift increases with k, thus the minimum close to $k = 10^{-1}$ probably corresponds to $\Delta\phi = 2\pi$, the minimum close to 19 cm^{-1} to 4π, and so on.

Thus a plot may be made of phase-shift wave number, as is shown in Fig. XI-3b. The closeness of the data points to a straight line indicates that the refractive index of polyethylene is constant within a few per cent in the spectral angle of $k = 15\text{-}50\ \text{cm}^{-1}$. From the slope of the line, the refractive index may be deduced because

$$\Delta\phi(k) = 2\pi|1-\text{Re}\ \mu|\ kL,$$

and the slope of Fig. XI-3b is given by

$$\frac{d}{dk}\Delta\phi(k) = 2\pi|1-\text{Re}\ \mu|\ L.$$

From Fig. XI-3b,

$$\frac{1}{2\pi}\frac{d}{dk}\Delta\phi(k) = \frac{5.0}{49.0}\ \text{radian cm},$$

and $2L = 0.213$ cm,

$$\therefore \qquad \text{Re}\ \mu = 1 + \left[\frac{5.0}{0.213 \times 49.0}\right]$$

$$= 1.48$$

which is in reasonable agreement with published values.

It should be noted that there is some deterioration in quality of the data of Fig. XI-3a in the spectral region between 30 cm^{-1} and 45 cm^{-1}. This is because of the presence of atmospheric water-vapor absorption lines that give rise to rather strong features in the spectrum, and as R(k) is obtained as the ratio of two spectra, the presence of the strong features will cause distortion such as that in Fig. XI-3a. By taking the average of several successive runs, however, this distortion is eliminated, as will be seen with the plasma data.

Figure XI-4 shows a typical response curve obtained with a real plasma, corresponding to a line density $3.1 \times 10^{14}\ \text{cm}^{-2}$; in this case $L = 7.5$ cm, so $N = 4.1 \times 10^{13}\ \text{cm}^{-3}$

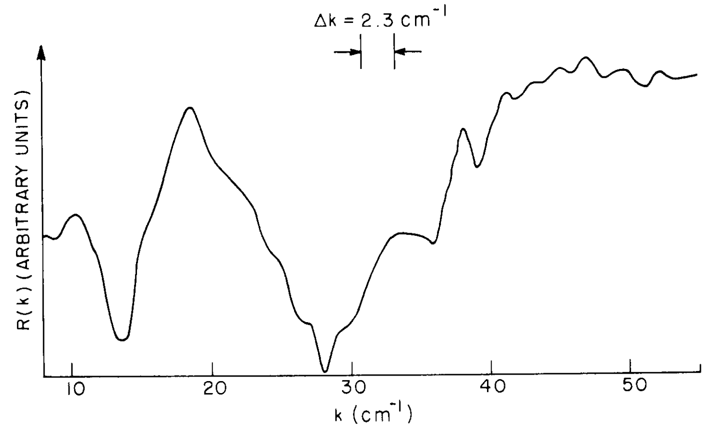

Fig. XI-4.
Typical interferometer response with a plasma. NL = 3.1×10^{14} cm^{-2}.

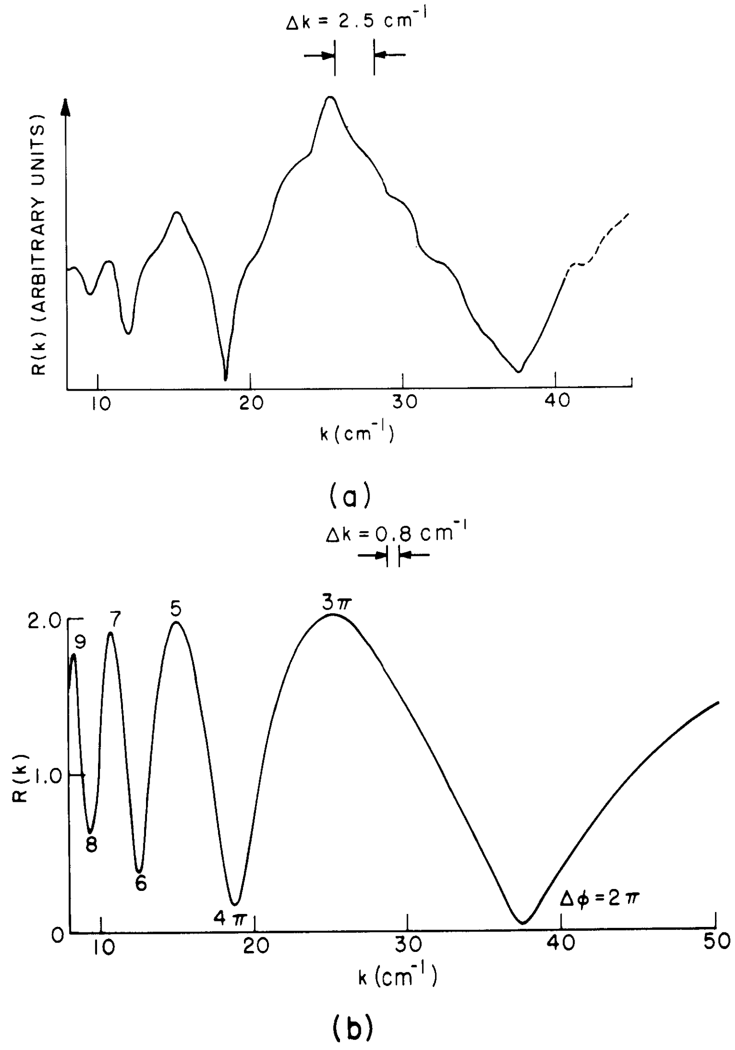

Fig. XI-5.

(a) Observed interferometer response resulting from plasma, where NL = 4.18×10^{14} cm^{-2}. (Average of 5 runs.)

(b) Theoretical interferometer response for plasma, where NL = 4.18×10^{14} cm^{-2}. [Compare with (a).]

and a central density of $N_o = 6.9 \times 10^{13}\ \text{cm}^{-3}$ can be expected. Distortion caused by water-vapor lines can also be seen in this response curve. Figure XI-5a shows a response curve attributable to a somewhat dense plasma ($NL = 4.18 \times 10^{14}$) which was obtained from the average of 5 similar interferograms. The quality of the data is substantially improved and the curve may be favorably compared with that of Fig. XI-5b, which shows the interferometer response computed from Eq. 10 which corresponds to the same value of NL, but with somewhat improved resolution and no attenuation resulting from the plasma. In this plasma $N = 5.6 \times 10^{13}\ \text{cm}^{-3}$, and $N_o = 9.3 \times 10^{13}\ \text{cm}^{-3}$.

In Fig. XI-6 the observed phase shift is plotted against wavelength, 1/k, to which it should bear a linear relationship (see Eq. 2). The fact that the data points very strongly suggest a straight line through zero indicates that the dominant observed phase shift is due only to the plasma and not to some spurious effect such as heating of the gas. This represents a distinct advantage of far infrared techniques over optical methods. At optical frequencies, the refractive index of the plasma is usually so small that it is of the same order of magnitude as the charge in refractive index of the background gas caused by heating from the plasma. Also, acoustic vibrations of the optical parts can cause effects of the same order of magnitude as that of the plasma.[13] Figure XI-6 indicates that for density measurements alone, phase-shift measurements at one frequency are sufficient.

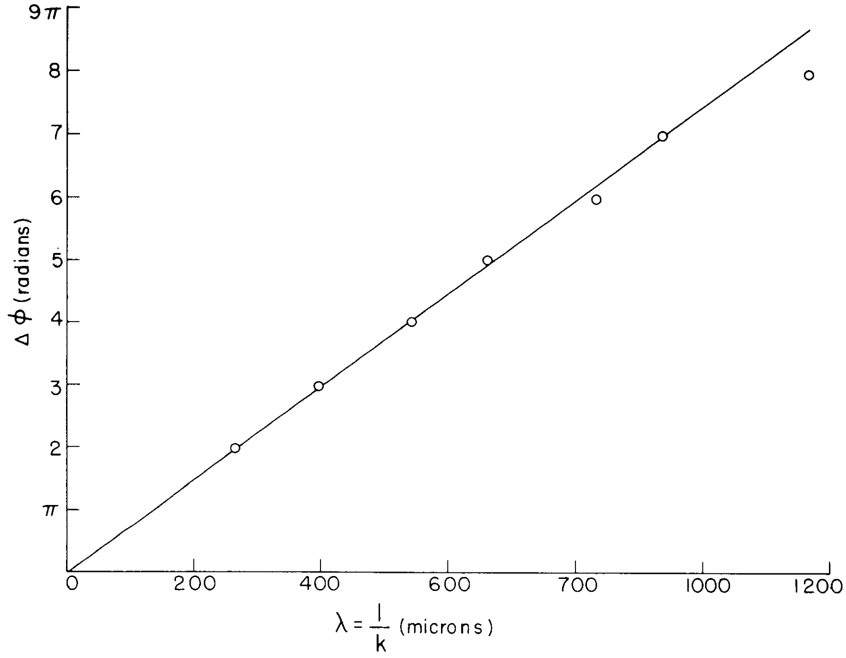

Fig. XI-6. Interpretation of Fig. XI-5a.

5. Resolution and Noise

As has been explained, the interferograms in this experiment always contain a phase term ϕ, as in Eq. 6. Thus both the sine and cosine Fourier transforms must be evaluated in order to avoid asymmetry in the final spectrum.[3, 14, 16] In this case the spectrum is obtained as the square root of the sum of the squares of the sine and cosine transforms:

$$S(k) = \int_0^D I(x)\, A\left(\frac{x}{D}\right) \sin (2\pi kx)\, dx$$

$$C(k) = \int_0^D I(x)\, A\left(\frac{x}{D}\right) \cos (2\pi kx)\, dx$$

$$\therefore \quad \mathscr{I}'(k) = \sqrt{S^2(k) + C^2(k)}$$
$$= \mathscr{I}(k') * \chi(k-k').$$

The function $A\left(\frac{x}{D}\right)$ is the apodizing function[5] and, in this case, is a triangle:

$$A\left(\frac{x}{D}\right) = \left(1 - \frac{x}{D}\right).$$

$\chi(k-k')$ is the scanning function, or instrumental line shape first mentioned above.

The instrumental line shape for this situation has been given analytically by Lowenstein[14] as

$$\chi^2(k) = \left\{ \frac{D}{4} \frac{\sin^2 [\pi(k-k_o)D]}{[\pi(k-k_o)D]^2} \right\}$$
$$+ \frac{1}{4\pi^2(k-k_o)^2} \left\{ 1 - \frac{\sin [2\pi(k-k_o)D]}{2\pi(k-k_o)\, D} \right\}$$
$$+ [\text{small terms in } (k+k_o)] \tag{11}$$

and it is illustrated in Fig. XI-7 where it was obtained by feeding 18.16 cycles of pure cosine to the computer program, simulating a monochromatic signal at $k = 30\ \text{cm}^{-1}$ with the same resolving power (that is, number of data points) that is used for the data presented in the previous section. This line shape has been discussed in detail by Connes,[3] who pointed out that the procedure of taking the sum of the squares of the two transforms is nonlinear. In this case random-noise fluctuations in the interferogram, instead of cancelling themselves out in the Fourier integrals, are always added cumulatively. For this reason, in cases in which the average of several runs is desired, it is important to

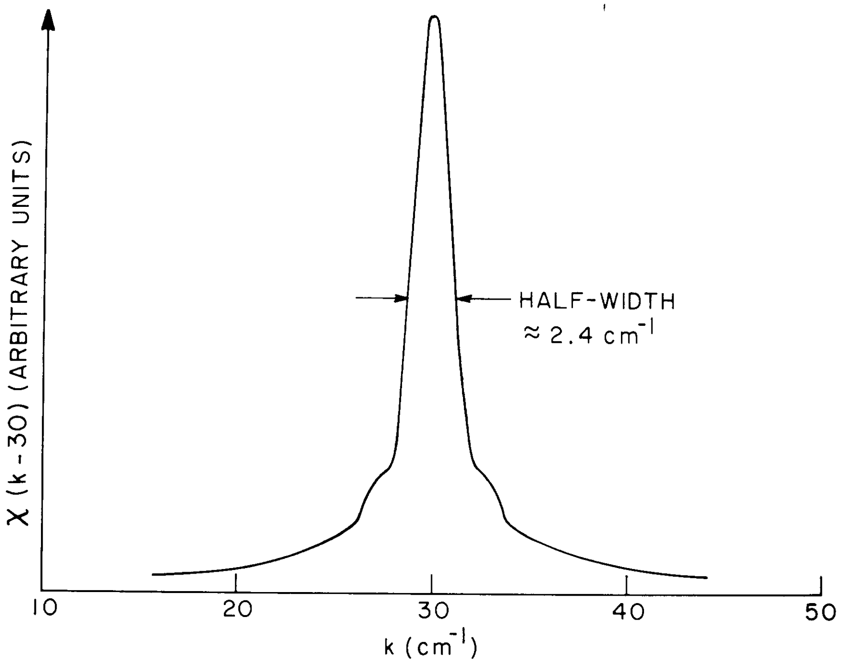

Fig. XI-7. Instrumental linewidth for k = 30 cm^{-1} (18.16 cycles of cosine at k = 30 cm^{-1}).

average the interferograms before performing the transformation, rather than to average the transformed spectra, because the noise in the spectra will not average to zero.

In addition to this disadvantage, the wings of the scanning function do not decay very rapidly; thus there is always a strong "background signal" in all parts of the spectrum. The function shows, however, a high degree of symmetry, and Eq. 11 contains no reference to the phase term in the interferograms, also there are no strong ripples in the wings on account of the triangle apodization.

As the phase terms in the interferograms are not known exactly, and vary over many multiples of π throughout the spectra, it would be exceedingly difficult to employ any of the phase correction methods described by Lowenstein,[14] Gibbs and Gebbie,[15] and Forman, et al.[15] The data presented in the previous section indicate that the scanning function is adequate in spite of its disadvantages.

The signal-to-noise ratio in the experiment is quite poor, even for a far infrared interferometer. This is because the beam is very narrow (dictating a small solid angle at the source); also the signal is sampled with a 3-μsec gate which leads to a further reduction of signal-to-noise ratio from that of a conventional chopping technique. A double RC filter (12 db/octave, $\tau = 3$ sec) was necessary to reduce the noise to an acceptable level. It has been mentioned that the signal was sampled at intervals of $\delta = 42.3$ microns path difference; this places certain requirements on the filtering system.

When the path difference is varied at a rate of v cm $\sec^{-1}$, it is clear that the infrared signal of wave number k becomes a signal of frequency $\omega = 2\pi vk$, and this is subject to filtering by the double RC filter which has a frequency response of

$$\frac{E_{out}}{E_{in}} = \frac{1}{1+(\omega\tau)^2}.$$

It is also clear that electronic noise of frequency, ω, will also be "seen," after the Fourier transformation, as infrared noise at $k = \frac{\omega}{2\pi v}$.

The sampling theorem of information theory[17] stipulates that no frequency must be present (in the sampled signal) greater than

$$\omega_{max} = \pi \frac{v}{\delta}$$

$$= \frac{\pi}{t}$$

where t secs is the sampling interval. In the present case,

$$\delta = 42.3$$

$$\therefore \quad k_{max} = \frac{1}{2 \times \delta}$$

$$= 118 \text{ cm}^{-1}.$$

This topic is treated with great thoroughness by Connes.[3]

The result is illustrated in Fig. XI-8 where the filter response has been translated to k-space by the transformation $\omega = 2\pi vk$, and superimposed upon the observed infrared spectrum between k = 8 and 55 cm^{-1} and the noise, which extends to wave numbers

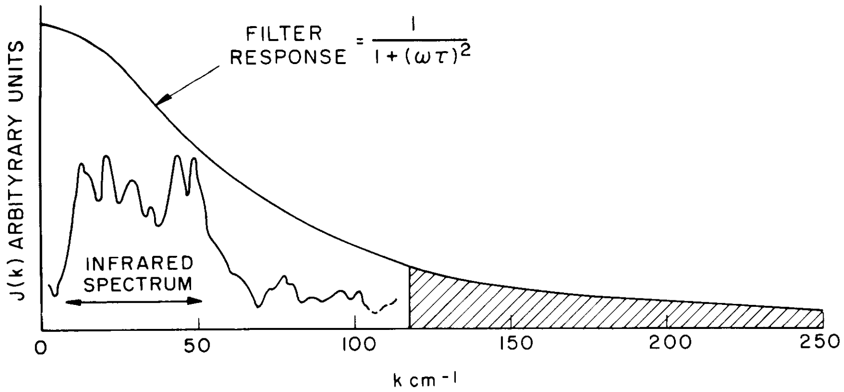

Fig. XI-8.

Frequency response of the double RC filter related to the observed spectrum (in wave numbers). $\tau = 3$ sec. $\omega = \frac{2\pi v}{R}$, where v is the rate of change of path difference (in this case, v = 8.6 microns $\sec^{-1}$).

greater than 55 cm^{-1}. It can be seen that the filtering is quite heavy for $k = 118\ cm^{-1}$ and suppresses the noise in this (shaded) region quite adequately for the data taken here, although part of the spectrum is also suppressed by the filter.

This technique is described in more detail, and its usefulness assessed, in the Author's doctoral thesis.[18]

D. T. Llewellyn-Jones

References

1. M. A. Heald and C. B. Wharton, Plasma Diagnostics with Microwaves (John Wiley and Sons, Inc., New York, 1965).
2. S. C. Brown, Basic Data of Plasma Physics (The Technology Press of M.I.T., Cambridge, Mass., and John Wiley and Sons, Inc., New York,1959).
3. J. Connes, Rev. Opt. 40, 45, 116, 171, 231 (1961). An English Translation of this fundamental text is available to Government Contractors as a U.S. Navy Publication NAV-WEPS Report No. 8099, NOTS TP 3157, published by the U.S. Naval Ordnance Test Station, China Lake, California.
4. P. L. Richards, J. Opt. Soc. Am. 54, 1474 (1964).
5. D. T. Llewellyn-Jones, Quarterly Progress Report No. 74, Research Laboratory of Electronics, M.I.T., July 15, 1964, pp. 81-89.
6. E. V. Lowenstein, Appl. Opt. 5, 845 (1966).
7. D. T. Llewellyn-Jones, S.M. Thesis, Department of Physics, Massachusetts Institute of Technology, June 1964.
8. F. A. Jenkins and H. E. White, Fundamentals of Optics (McGraw-Hill Book Company, New York, 1963).
9. S. C. Brown, G. Bekefi, and R. E. Whitney, J. Opt. Soc. Am. 53, 448 (1963).
10. D. T. Llewellyn-Jones, Quarterly Progress Report No. 80, Research Laboratory of Electronics, M.I.T., January 15, 1966, pp. 85-89.
11. J. C. Ingraham and J. J. McCarthy, Quarterly Progress Report No. 64, Research Laboratory of Electronics, M.I.T., January 15, 1962, pp. 76-79.
12. P. A. Crisman and others, "The Compatible Time-Sharing System, A Programmer's Guide" (The M.I.T. Press, Cambridge, Mass., 1965).
13. E. B. Hooper, Ph.D. Thesis, Department of Physics, Massachusetts Institute of Technology, September 1965.
14. E. V. Lowenstein, Appl. Opt. 2, 491 (1963).
15. M. L. Forman, W. H. Steel, and G. A. Vanasse, J. Opt. Soc. Am. 56, 59 (1966).
16. J. E. Gibbs and H. A. Gebbie, Infrared Phys. 5, 187 (1965).
17. S. Goldman, Information Theory (Prentice-Hall, Inc., Englewood Cliffs, N.J., 1962).
18. D. T. Llewellyn-Jones, Ph.D. Thesis, Department of Physics, Massachusetts Institute of Technology, February 1967.

C. ELECTRON DENSITY MEASUREMENTS WITH A NARROW-BAND FAR INFRARED INTERFEROMETER

In order to measure the electron concentration in high electron density plasmas, a narrow-band far infrared interferometer has been constructed to operate in the wavelength region of a few hundred microns. The initial instrument was conceived by Sanborn C. Brown,[1] and requires only a simple analysis of the output to obtain the desired data. Now, a new interferometer has been designed to operate with repetitively pulsed plasmas, retaining the same analysis for the data and a wavelength range of 200-400 microns. It is constructed in an open U frame to accommodate different plasma vacuum systems, and has a narrower bandwidth, which permits measurement of the increased electron densitites that are found in pulsed, as compared with steady-state, plasmas.

The interferometer can be viewed schematically as in Fig. XI-9; it is a symmetric two-beam instrument that can be compared roughly to a Rayleigh interferometer, except for the beam-splitting and recombining method. Far infrared radiation emitted from the high-pressure Hg arc source is focused by the entrance mirror at a distance equal to the path length to the far mirrors. This radiation falls first on grating No. 1 normal to its surface and is diffracted so that the plus and minus first orders of the desired radiation fall on the far mirrors. Thus the tunable lamellar reflection grating[2] and far mirrors form a monochrometer, or filter, the operating frequency being determined by the grating spacing and angle of the far mirrors with the grating normal. Radiation incident on the far mirrors is now returned to grating No. 2, that from the sample arm having passed twice through the plasma. Since the concave far mirrors have a radius of curvature equal to their distance from the gratings, the first grating is imaged on the second. Both the phase difference between the two beams returning to grating No. 2, which fixes the radiation pattern on the grating surface, and the lateral (direction indicated by arrow in Fig. XI-9) displacement of grating No. 2 with respect to grating No. 1 determine the output normal to grating No. 2. This output is then focused by the exit mirror on the detector. The important relation of output as a function of phase difference between the two arms and lateral movement of grating No. 2, which allows the phase shift by the plasma to be measured by moving this grating can be found through the following analysis of the optical system.

For simplicity, the optical system of the interferometer can be represented as the lens system in Fig. XI-10. When making actual calculations the proper geometry of the mirror system will be used. Now the modified Kirchhoff formulation of Bekefi,[3] which gives a good representation of the wave in the intermediate and far fields by microwave measurements, can be utilized. Under the assumption of an exponential ($-i\omega t$) time dependence of the wave, the spatial magnitude

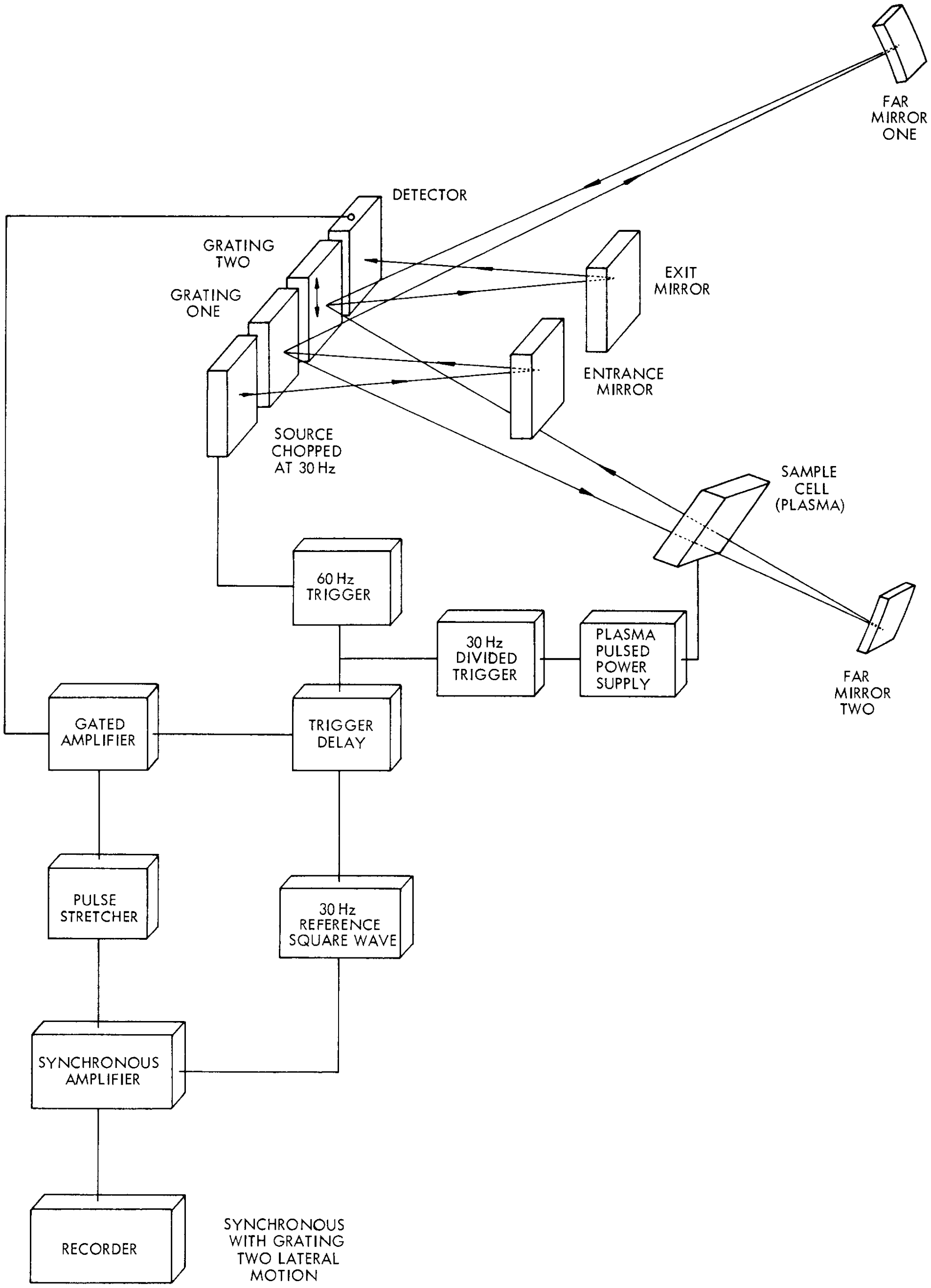

Fig. XI-9. Schematic representation of the interferometer and associated electronics equipment.

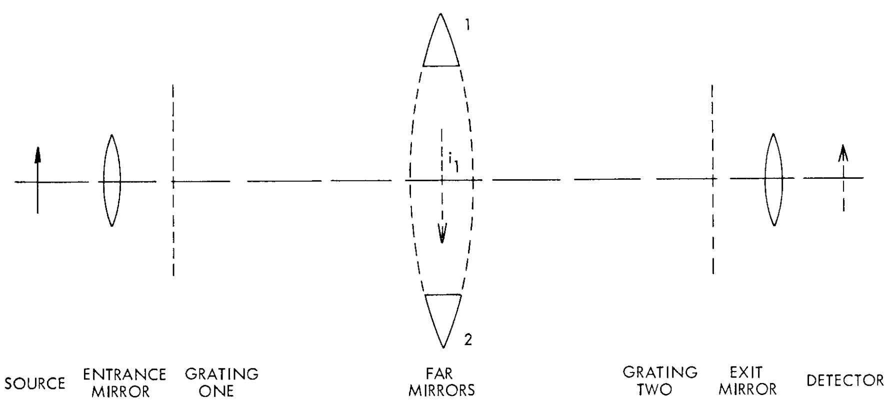

Fig. XI-10. Simplified lens approximation to the interferometer optics.

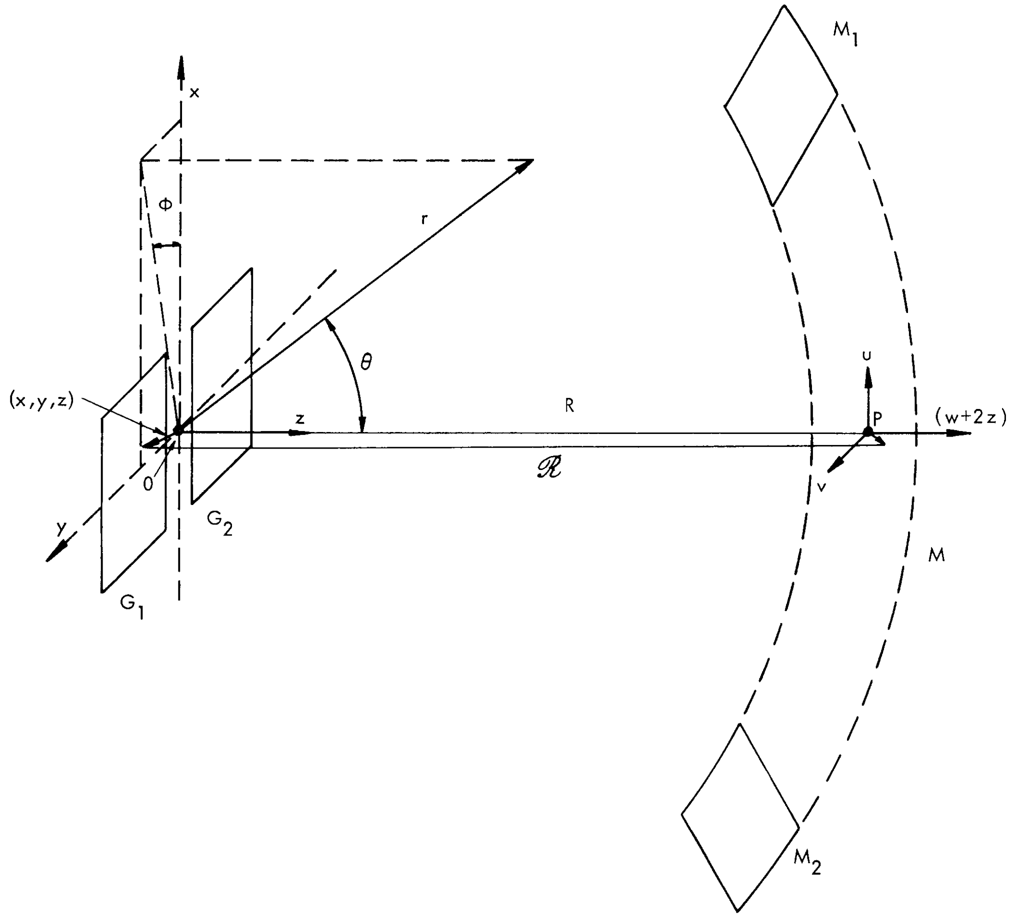

Fig. XI-11. Coordinate systems for the actual geometry of the interferometer, where G_1 and G_2 are the gratings, and the spherical surface of the far mirrors, M, has radius R and center O.

and phase at observation point Q is given by

$$U_{(Q)} = \frac{1}{2\pi}\int_A U_i \frac{\partial}{\partial n}\frac{e^{iks}}{s}\,dS,$$

where A is the surface at which diffraction is occurring, dS is an element in that surface, $\partial/\partial n$ is the normal derivation with the unit vector normal to A at dS used, U_i is the phase and magnitude of the wave front incident on dS, k is the propagation constant ω/c, and s is the distance from dS to Q. Henceforth the complex U will be called the amplitude of the wave containing both phase and magnitude. Under the assumption that diffraction effects from the entrance mirror are negligible, there is a converging spherical wave front incident on grating 1 directed as if to converge at the far mirror surface (dotted image i_1 in Fig. XI-10). By entering the amplitude of this wave at grating 1 into the equation above, the amplitude at the surface of the far mirror can be found, and, by iterating again with this new amplitude, the radiation amplitude falling on grating 2 can be determined. This process could be continued right up to the detector but instead a simplification that obviates the complications of diffraction from the exit mirror can be employed, which should have negligible effects, and the integrated amplitude at the detector can be found directly.

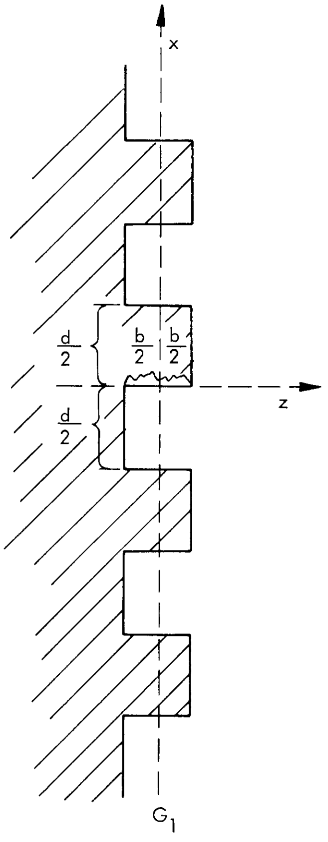

Fig. XI-12. Cross section of the grating profile.

Now, carrying out these steps with the actual mirror geometry of the interferometer and utilizing the standard coordinates indicated in Fig. XI-11, we find that the incident amplitude of the converging spherical wave from the source and entrance mirror at the grating plane G_1 is

$$U_{G_1} = u\,\frac{e^{-ik\mathcal{R}}}{\mathcal{R}},$$

where u is an constant proportional to the magnitude of the incident radiation, and $\mathcal{R}$ is the distance from grating 1 to the point of convergence. In the case of the center point of the source and where the surface lies on G_1 (the x-y plane of the gratings) the point of convergence is P lying on the spherical surface M of the far mirror. Actually, the grating surface has grooves so that the reflected convergence point of the incoming wave changes, and this must be accounted for in $\mathcal{R}$. Therefore,

$$\mathcal{R} = \left[(u-x)^2+(v-y)^2+(\omega+R+z)^2\right]^{1/2},$$

where (u, v, ω) is the point in the undistorted image of the source, and (x, y, z) is the point on the grating surface defined relative to the plane G_1 as indicated in Fig. XI-12.

The first step gives the amplitude at the far mirror,

$$U_M = \frac{1}{2\pi} \int_{G_1} U_{G_1} \frac{d}{dz} \frac{e^{iks}}{s} \, dxdy,$$

where s is the distance from a point on the far mirror (R, θ, ϕ) and a point on grating 1, that is,

$$s = \left[(R \cos \phi \sin \theta - x)^2 + (R \sin \phi \sin \theta - y)^2 + (R \cos \theta - z)^2\right]^{1/2}.$$

To differentiate between the two far mirrors, a phase shift from the plasma is included by multiplying U_{M_2} by $e^{i\Phi}$. Next, from U_M the amplitude at the second grating is determined, again including the plasma phase shift:

$$U_{G_2} = -\frac{1}{2\pi} \int_{M_1} U_{M_1} \frac{d}{dR} \frac{e^{iks'}}{s'} R^2 \sin \theta \, d\theta d\phi$$

$$-\frac{e^{i\Phi}}{2\pi} \int_{M_2} U_{M_2} \frac{d}{dR} \frac{e^{iks'}}{s'} R^2 \sin \theta \, d\theta d\phi,$$

where

$$s' = \left[R \cos \phi \sin \theta - x'\right)^2+(R \sin \phi \sin \theta - y')^2+(R \cos \theta - z')^2]^{1/2},$$

the coordinates (x', y', z') define a point on G_2, and

$$\Phi = k \int_0^L \left[1 - \left(1 - \frac{\omega_p^2(\ell)}{\omega^2}\right)^{1/2}\right] d \,,$$

ω_p being the plasma frequency proportional to the square root of the electron density.

In the final step, diffraction by the exit mirror is neglected. Since the exit mirror is positioned to focus radiation on the center of the detector head, as if it came from P and reflected off the grating plane, any radiation from G_2 that goes to the detector will look as if it came from P (correcting, of course, for the grating groove depth). Now radiation from P focused on D must all travel the same optical path length so that for radiation concentrated on the detector the path length PG_2 plus G_2D equals a constant. The amplitude at the detector can be found by summing all of the amplitudes of the radiation from G_2 multiplied by their phase shifts resulting from path length G_2D (or minus PG_2 and dropping the constant phase shift). Therefore,

$$U_D = \frac{1}{A_{G_2}} \int_{G_2} U_{G_2}\, e^{-ik\mathcal{R}'}\, dx'dy',$$

where A_{G_2} is the illuminated area of G_2, and

$$\mathcal{R}' = \left[(u-x')^2+(v-y')^2+(\omega+R+z')^2\right]^{1/2}.$$

The total integral now is

$$\begin{aligned} U_D = -\frac{1}{4\pi^2 A_{G_2}} \int_{G_2} e^{-ik\mathcal{R}'}\, dx'dy' \Bigg\{ &\int_{M_1} \frac{d}{dR}\left(\frac{e^{iks'}}{s'}\right) R^2 \sin\theta\, d\theta d\phi \int_{G_1} \frac{e^{-ik\mathcal{R}}}{\mathcal{R}} \frac{d}{dx}\left(\frac{e^{iks}}{s}\right) dxdy \\ &+ e^{i2\Phi} \int_{M_2} \frac{d}{dR}\left(\frac{e^{iks'}}{s'}\right) R^2 \sin\theta\, d\theta d\phi \int_{G_1} \frac{e^{-ik\mathcal{R}}}{\mathcal{R}} \frac{d}{dz}\left(\frac{e^{iks}}{s}\right) dxdy \Bigg\}. \end{aligned}$$

Carrying out the differentiation and dropping additives terms smaller by $\frac{\lambda}{R} \approx 3 \times 10^{-4}$, we obtain

$$\begin{aligned} U_D = \frac{1}{4\pi^2 A_{G_2}} \Bigg\{ &\int_{M_1} R^2 \sin\theta\, d\theta d\phi \int_{G_2} e^{ik(s'-\mathcal{R}')} \frac{ik}{s'^2} \\ &\cdot \left[R-(x'\cos\phi\sin\theta + y'\sin\phi\sin\theta + z'\cos\theta)\right] dx'dy' \int_{G_1} e^{ik(s-\mathcal{R})} \frac{ik}{\mathcal{R}s^2} \left[R\cos\theta - z\right] dxdy \\ &+ e^{i2\Phi} \int_{M_2} R^2 \sin\theta\, d\theta d\phi \int_{G_2} e^{ik(s'-\mathcal{R})} \frac{ik}{s'^2} \\ &\cdot \left[R-(x'\cos\phi\sin\theta + y'\sin\phi\sin\theta + z'\cos\theta)\right] dx'dy' \int_{G_1} e^{ik(s-\mathcal{R})} \frac{ik}{\mathcal{R}s^2} \left[R\cos\theta - z\right] dxdy \Bigg\}. \end{aligned}$$

By including a z dimension in $\mathcal{R}$, $\mathcal{R}'$, s and s', the surfaces G_1 and G_2 really become the grating surfaces, so that each G integral can be broken up into an integral over the front flat surfaces of the grating and the depressed surfaces. Thus

$$\int_{G_1} e^{ik(s-\mathcal{R})} \frac{ik}{\mathcal{R}s^2} [R\cos\theta - z]\,dxdy = \sum_{\substack{n=-N/2\\(z=b/2)}}^{N/2} \int_{nd}^{(n+1/2)d} dx \int_{y_1}^{y_2} dy\; e^{ik(s-\mathcal{R})} \frac{ik}{\mathcal{R}s^2}\left[R\cos\theta - \frac{b}{2}\right]$$

$$+ \sum_{\substack{n=-N/2\\(z=-b/2)}}^{N/2} \int_{(n-1/2)d}^{nd} dx \int_{y_1}^{y_2} dy\; e^{ik(s-\mathcal{R})} \frac{ik}{\mathcal{R}s^2}\left[R\cos\theta + \frac{b}{2}\right]$$

where the grating is positioned relative to the z-axis, as indicated in Fig. XI-12, N is the number of grooves in the grating, d is the grating spacing, and (y_2-y_1) is the grating width. For the G_2 integral, the lateral, or x, position of the grating relative to G_1 must be taken into account and, since the image of G_1 on G_2 from the far mirror is inverted, the zero position for G_2 will be the inverse of Fig. XI-12.

$$\int_{G_2} e^{ik(s'-\mathcal{R}')} \frac{ik}{s'^2} [R-(x'\cos\phi\sin\theta + y'\sin\phi\sin\theta + z'\cos\theta)]\,dx'dy'$$

$$= \sum_{\substack{n=-N/2\\(z'=b/2)}}^{N/2} \int_{(n-1/2)d+\Delta}^{nd+\Delta} dx' \int_{-y_2}^{-y_1} dy'\; e^{ik(s'-\mathcal{R}')} \frac{ik}{s'^2}$$

$$\cdot \left[R-\left(x'\cos\phi\sin\theta + y'\sin\phi\sin\theta + \frac{b}{2}\cos\theta\right)\right]$$

$$+ \sum_{\substack{n=-N/2\\(z'=-b/2)}}^{N/2} \int_{nd+\Delta}^{(n+1/2)d+\Delta} dx' \int_{-y_2}^{-y_1} dy'\; e^{ik(s'-\mathcal{R}')} \frac{ik}{s'^2}$$

$$\cdot \left[R-\left(x'\cos\phi\sin\theta + y'\sin\phi\sin\theta - \frac{b}{2}\cos\theta\right)\right],$$

where Δ is the lateral distance G_2 is moved.

To solve these integrals analytically to first order, $\mathcal{R}$, $\mathcal{R}'$, s and s' must be expanded in decreasing powers of R. Terms of relative order $1/R^2$ and higher are neglected in the exponential, and other integrated terms of $1/R$ and higher are neglected. From the symmetry of the interferometer about the (y, z)-plane the two far mirror integrals can be combined by letting ϕ in the M_2 integral go to $(\phi'+180°)$, so that the limits of integration for the two integrals are identical. Dropping constant phase factors and the prime on the dummy ϕ variable,

$$U_D = \frac{k^2(y_2-y_1)\,d}{2\pi R(N+1)} \int_{M_1} \sin\theta\, d\theta d\phi \left\{ \frac{\sin^2\left[(N+1)\,k\,\frac{d}{2}\cos\phi\sin\theta\right]}{\sin^2\left[k\,\frac{d}{2}\cos\phi\sin\theta\right]} \times \frac{\sin^2\left[k\,\frac{d}{4}\cos\phi\sin\theta\right]}{\left[k\,\frac{d}{4}\cos\phi\sin\theta\right]^2} \right.$$

$$\times \frac{\sin^2\left[k\left(\frac{y_2-y_1}{2}\right)\sin\phi\sin\theta\right]}{\left[k\left(\frac{y_2-y_1}{2}\right)\sin\phi\sin\theta\right]^2} \times \cos\left[k\Delta\cos\phi\sin\theta + \Phi\right]$$

$$\times \cos\left[k\,\frac{d}{4}\cos\phi\sin\theta + k\,\frac{b}{2}(1+\cos\theta)\right] \times \cos\left[k\,\frac{d}{4}\cos\phi\sin\theta - k\,\frac{b}{2}(1+\cos\theta)\right]\ . \qquad (1)$$

The factors in the integrand are equivalent to those of a typical Fraunhoffer analysis, but it should be stressed that the approximations alone did not bring about this similarity – rather, it resulted from the fact that the symmetry of the interferometer causes the first power R terms in the exponentials to cancel exactly.

This integral cannot be easily evaluated in exact form, but by noting that the first term in the bracket of Eq. 1 is a strongly peaked function, it can be replaced by a delta function at these peaks and there by give a good idea of the solution of the integral.

$$\frac{\sin^2\left[(N+1)\,k\,\frac{d}{2}\cos\phi\sin\theta\right]}{\sin^2\left[k\,\frac{d}{2}\cos\phi\sin\theta\right]} \longrightarrow \frac{(N+1)\pi}{k\,\frac{d}{2}\cos\phi}\,\delta\left(\sin\theta - \frac{2m\pi}{kd\cos\phi}\right),$$

where m is the order of diffraction.

$$U_D = -\frac{8}{\pi^2 R}\cos\left[2\pi m\frac{\Delta}{d} + \Phi\right] \int_{\phi_1}^{\phi_2} \frac{\sin^2\left[\pi m\left(\frac{y_2-y_1}{d}\right)\tan\phi\right]}{\left[\pi m\left(\frac{y_2-y_1}{d}\right)\tan\phi\right]^2}\,\pi m\left(\frac{y_2-y_1}{d}\right) d\tan\phi$$

$$\times \begin{Bmatrix} 1, & \text{for } \theta_1 < \theta < \theta_> \\ 0, & \text{for all other } \theta \end{Bmatrix} \times \begin{cases} \frac{1}{m^2}\sin^2\left[k\,\frac{b}{2}(1+\cos\theta)\right], & m \text{ odd} \\ \cos^2[kb], & m = 0 \\ 0, & m \text{ even} \end{cases}$$

where the far mirrors lie between θ_1 and θ_2. From this and the fact that $I_D = U_D^* U_D$, it follows that the intensity at the detector is

$$I_D = \frac{2^6}{\pi^4 R^2} \cos^2\left[2\pi m \frac{\Delta}{d} + \Phi\right] \left\{\int_{\alpha_1}^{\alpha_2} \left(\frac{\sin \alpha}{\alpha}\right)^2 dx\right\}^2$$

$$\times \begin{cases} 1, & \text{for } \theta_1 < \theta < \theta_2 \\ 0, & \text{for all other } \theta \end{cases} \times \begin{cases} \dfrac{1}{m^4} \sin^4\left[k \dfrac{b}{2}(1+\cos\theta)\right], & m \text{ odd} \\ \cos^4 [kb], & m = 0 \\ 0, & m \text{ even} \end{cases}$$

where $\alpha = \pi m\left(\frac{y_2 - y_1}{d}\right) \tan \phi$. Note that the grating depth b is so set that the first order is maximized; $k\frac{b}{2}(1+\cos\theta) = \frac{\pi}{2}$. Now, the relation between the lateral displacement Δ and the single-pass plasma phase shift, Φ, is clear; if the grating is driven laterally as a function of time and the plasma is turned on, the shift in the sinusoidal output at this time is a measure of Φ.

Actually, I_D is not the signal seen by the detector. Since the detector integrates over frequency its signal is

$$\mathscr{I}_D = \left|\int F(k)\, U_D(k)\, dk\right|^2 = |\mathscr{U}_D|^2,$$

where F(k) is the normalized frequency envelope determined by detector sensitivity, source output, window thin-film effects, and so forth.

$$\mathscr{U}_D = U_o \int_0^\infty F'(k) \cos\left[2\pi \frac{\Delta}{d} + \Phi(k)\right] dk,$$

where U_o equals all of U_D, except the cosine function in the integrand above and the term involving θ_1 and θ_2, which limits the values of k accepted by the interferometer. Again, F'(k) is normalized so that its integral over k is unity. Expanding $\Phi(k)$ about some k_o by the Taylor series and considering the first two terms, if k_o is so defined that

$$\int_0^\infty F'(k) \sin\left[\left(\frac{d\Phi}{dk}\right)_{k_o} (k-k_o)\right] dk = 0,$$

we obtain

$$\mathscr{U}_D = U_o \cos\left[2\pi \frac{\Delta}{d} + \Phi(k_o)\right] \int_0^\infty F'(k) \cos\left[\left(\frac{d\Phi}{dk}\right)_{k_o} (k-k_o)\right] dk.$$

The modulation will disappear with reasonable F'(k) envelopes if

$$\left(\frac{d\Phi}{dk}\right)_{k_o} \delta k > \frac{\pi}{2},$$

where δk is the half-width at half-maximum. For a plasma for which the phase shift is inversely proportional to k, this limit is

$$\Phi\left(\frac{\delta k}{k}\right) > \frac{\pi}{2}.$$

Thus we see there is a limitation on the measurable phase shift, because of dispersion of the medium and the accepted bandwidth.

Turning now to the experimental measurments on the interferometer itself without a plasma, we found that when properly aligned the lateral motion of G_2 could give a 75% modulation signal. Figure XI-13 shows a run with over 60% modulation. The output bandwidth of the interferometer was measured by placing a modified Perkin-Elmer monochrometer between its output and the detector; this, with $\theta = 7°$ for the center of the far mirror, gave a center wavelength of 197 μ and a half-width at half-maximum or bandwidth of 5%. Using different thicknesses of the rather nondispersive medium, polyethylene, we measured the modulation magnitude as a function of phase shift (Fig. XI-14), From the index of refraction of polyethylene, n = 1.47 at $\lambda \approx 200\ \mu$, the center frequency and bandwidth from phase shift and modulation magnitude measurements were in good agreement with those made with the monochrometer.

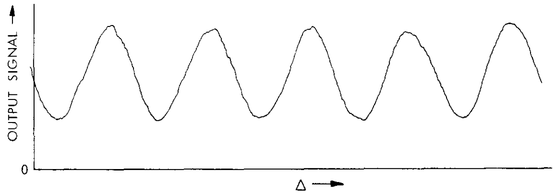

Fig. XI-13.

Typical modulation as a function of lateral motion by grating 2 with polyethlene in one arm.

The plasma tube that is now being used with the interferometer consists of coaxial cylindrical electrodes; the outer solid cylinder is a stainless-steel cathode, and the inner transparant grid cylinder is a stainless-steel anode. A 35 μsec kV pulse at a 30-cycle rate produces a negative glow that fills the inside of the anode with pressures of a few Torr of helium. The Pyrex end plates of the cylinder have crystal-quartz windows set into their center, which allows the infrared to propagate through the plasma

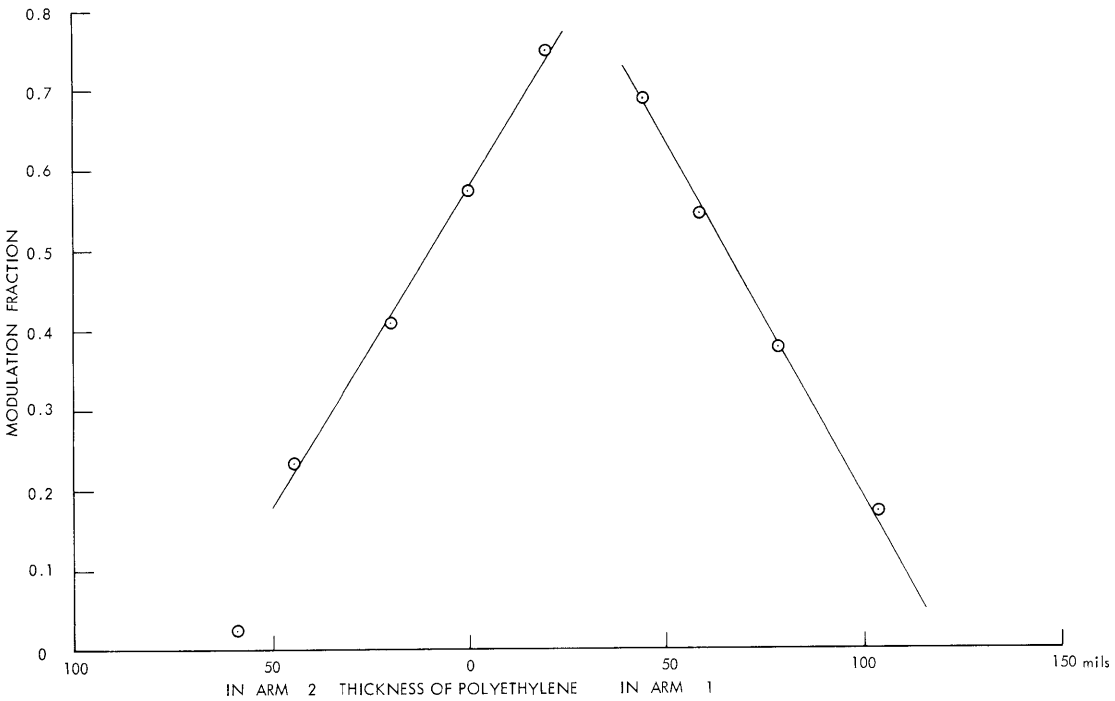

Fig. XI-14. Modulation magnitude as a function of phase shift from polyethlene sheets.

along the axis of the cylinders. As shown schematically in Fig. XI-9, the electronics part consists of a 3-μsec sampling gate at a 60-cycle rate, which can be moved in time relative to the plasma pulse. This sampled signal is then stretched to fill the time between gates, thereby giving a square wave whose amplitude is the difference between the infrared signal in the afterglow of the plasma and the noise when there is neither plasma nor infrared (cut out by a synchronous 30-cycle chopper). Finally, synchronous detection is used to give this square-wave amplitude, which is plotted on a recorder whose drive is synchronized with the lateral movement of G_2. A few phase-shift determinations have been made on the plasma, and average electron densities over the path length of plasma have been measured to be 5×10^{13} electrons per cubic centimeter in the early afterglow.

M. L. Andrews

References

1. S. C. Brown, G. Bekefi, and R. E. Whitney, J. Opt. Soc. Am. 53, 448 (1963).
2. M. L. Andrews, Quarterly Progress Report No. 74, Research Laboratory of Electronics, M.I.T., July 15, 1964, pp. 74-78.
3. G. Bekefi, Studies in Microwave Optics No. 38, The Eaton Electronics Research Laboratory, McGill University, 1957, p. 14.

D. MICROWAVE SCATTERING FROM WARM PLASMA WAVES NEAR THE ELECTRON CYCLOTRON FREQUENCY

We have observed microwave scattering from density oscillations in an electron-beam produced plasma. Large-amplitude emission of microwave radiation associated with these density oscillations was also observed, and the nature of the frequency spectrum of this radiation indicates that the density oscillations were associated with unstable warm plasma waves. We shall give a brief summary of previous work on these waves, after which our radiation measurements and the microwave scattering experiment will be described.

During the last few years, a great deal of theoretical and experimental work has been devoted to the study of waves that propagate in a warm plasma in a magnetic field. The effects of these waves were first observed experimentally in the form of anomalous peaks in the frequency spectrum of radiation emitted from laboratory plasmas at the electron-cyclotron frequency and its harmonics.[1,2] The origin of this radiation was not known at the time, but it is now generally accepted that it is due to longitudinal waves propagating in a warm plasma in a magnetic field. These waves can become unstable when a group of electrons with a large component of velocity perpendicular to the magnetic field is present in a thermal plasma. Some of the plasma wave energy can be emitted in the form of electro-magnetic radition, but the mechanism for this coupling is not yet completely understood.

The dispersion relation for the propagation of these modes in a Maxwellian plasma was derived by Bernstein.[3] It was suggested by Canobbio and Croci[4] that fast electrons could excite these waves, and a derivation of conditions for instability and growth rates was given by Crawford and Tataronis.[5]

It was first noted by Lustig, McBee, and Kalisky[6] that the anomalous radiation could be emitted at frequencies slightly different from the cyclotron harmonics, and the emission of radiation away from $n\omega_c$ was observed even more clearly by Tanala, Mitani, and Kubo.[7] They measured the radiation emitted from a discharge in Neon at a pressure of 1.25×10^{-1} mm Hg. Measurements were taken at a fixed frequency of 9500 Mc, and the magnetic field was varied. They observed a peak in the microwave emission which for very small discharge currents was at a magnetic field corresponding to $\omega/\omega_c \approx 1$, where ω_c is the electron-cyclotron frequency, and ω is the receiver frequency. As the discharge current was increased, this peak shifted to lower magnetic fields, until at high discharge currents, $i_d > 0.5$ amp, the radiation peak was at $\omega/\omega_c \lesssim 2$. Thus the peak in microwave emission had shifted continuously from the cyclotron frequency to the second harmonic of the cyclotron frequency. At very low discharge currents, only this peak, $1 < \omega/\omega_c < 2$, was observed, but as the discharge current increased, peaks appeared between each of the higher harmonics and shifted upward in frequency, approaching $\omega/\omega_c \approx n$, for large discharge currents, where $n = 3, 4, 5, \ldots$, up to $\sim n = 10$.

The data of Tanaka and co-workers can be explained in terms of Bernstein's theory[3] for longitudinal waves propagating perpendicularly to the magnetic field. For very small electron densities, $\omega/\omega_c \ll 1$, his dispersion relation shows modes of propagation existing at $n\omega_c$, $n = 1, 2, 3, \ldots$. As ω_p gets larger, the frequencies of propagation increase toward the next higher harmonic, $(n+1)\omega_c$.

Observations of the emission of microwave radiation at frequencies near but not exactly equal to $n\omega_c$ were also made by Bekefi and Hooper,[8] who measured the radiation from an electron-beam produced plasma. Near each harmonic, $\omega = n\omega_c$ $(n = 1, 2, 3, \ldots)$, two radiation peaks were observed, one of which originated from the beam electrons and was Doppler-shifted. The other peak was not Doppler-shifted but was shifted from $\omega = n\omega_c$ toward a higher frequency by an amount proportional to the electron-beam density. This second peak seems to be related to an unstable Bernstein mode, since for each of the harmonics the peak shifts to higher frequencies with increasing electron density, as expected from the dispersion relation for these modes.

The experimental work that we wish to report here has two parts, and the two experimental geometries are shown in Fig. XI-15. Measurements of the microwave power emitted by the plasma were made with the geometry shown in Fig. XI-15a, and the scattering experiment was done with the geometry shown in Fig. XI-15b.

The plasma was produced by firing the electron beam from a focused Pierce-type gun into mercury vapor at a pressure of 2×10^{-4} mm Hg. The axis of the plasma tube was aligned along a uniform magnetic field, but the electron gun was outside the field so that the electrons in the beam acquired transverse energy as they entered the magnetic field. Measurements of the microwave power emitted by the plasma were made by passing the tube through an S-band waveguide, as shown in Fig. XI-15a, and feeding the microwaves to an S-band radiometer tuned to 3000 Mc. This experimental geometry was the same as that of Bekefi and Hooper,[8] except that their waveguide was oriented with its axis approximately parallel to the axis of the tube. We varied the magnetic field and plotted the microwave power emitted at the fixed radiometer frequency (3000 Mc) against B. As did Bekefi and Hooper,[8] we found peaks in the microwave radiation for frequencies in the neighborhood of $n\omega_c$ $(n = 1, 2)$. Near each harmonic two peaks were observed. One was of relatively low amplitude and very nearly at $\omega = n\omega_c$; the other much larger in amplitude, was observed to shift away from $n\omega_c$ toward higher frequencies as the beam voltage was increased. (Increasing the beam voltage also increased the beam density and the plasma density.) Figure XI-16 shows the frequency shifts of these peaks for the first two harmonics. The solid lines represent the large-amplitude peaks, and the dashed lines, represent the low-amplitude peaks. Again, as in the experiments of Bekefi and Hooper,[8] and Tanaka and co-workers,[7] we have a radiation

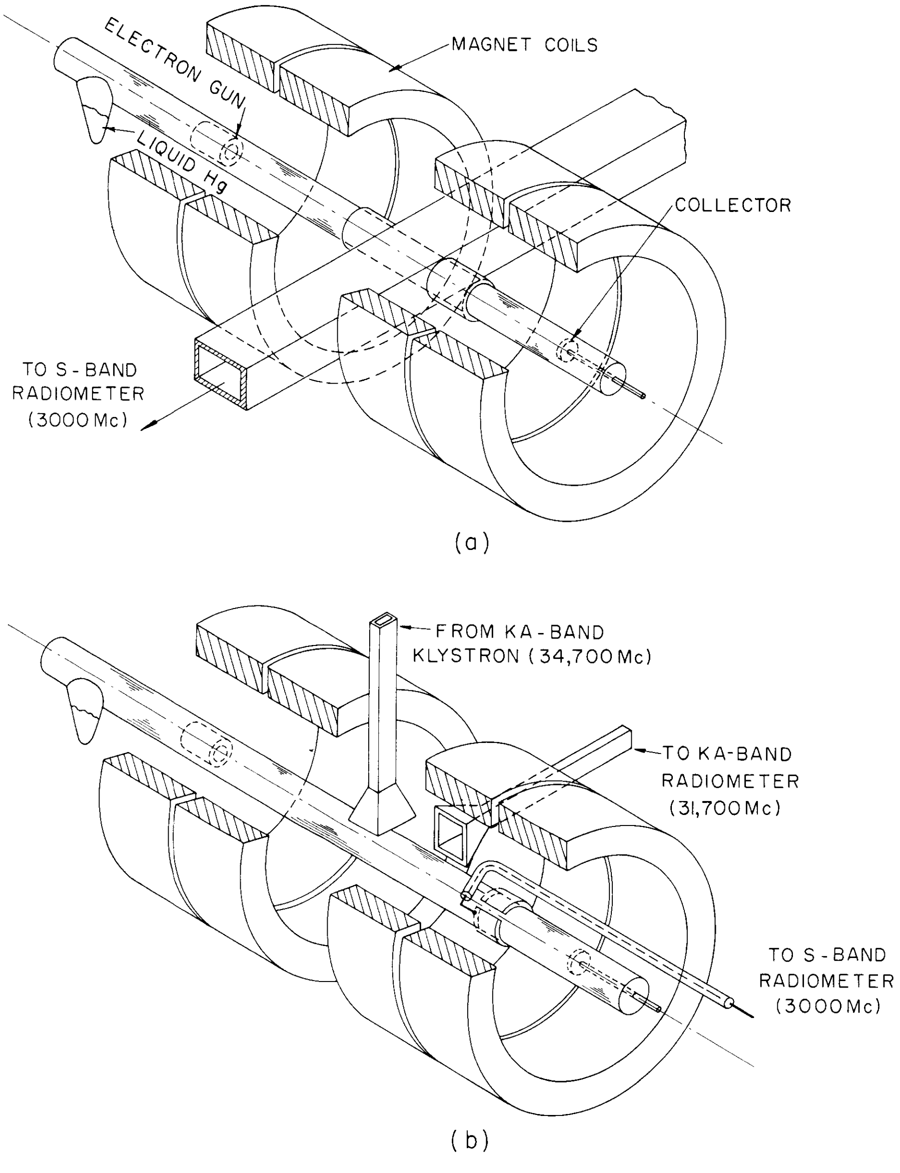

(a)

(b)

Fig. XI-15. Experimental geometry.

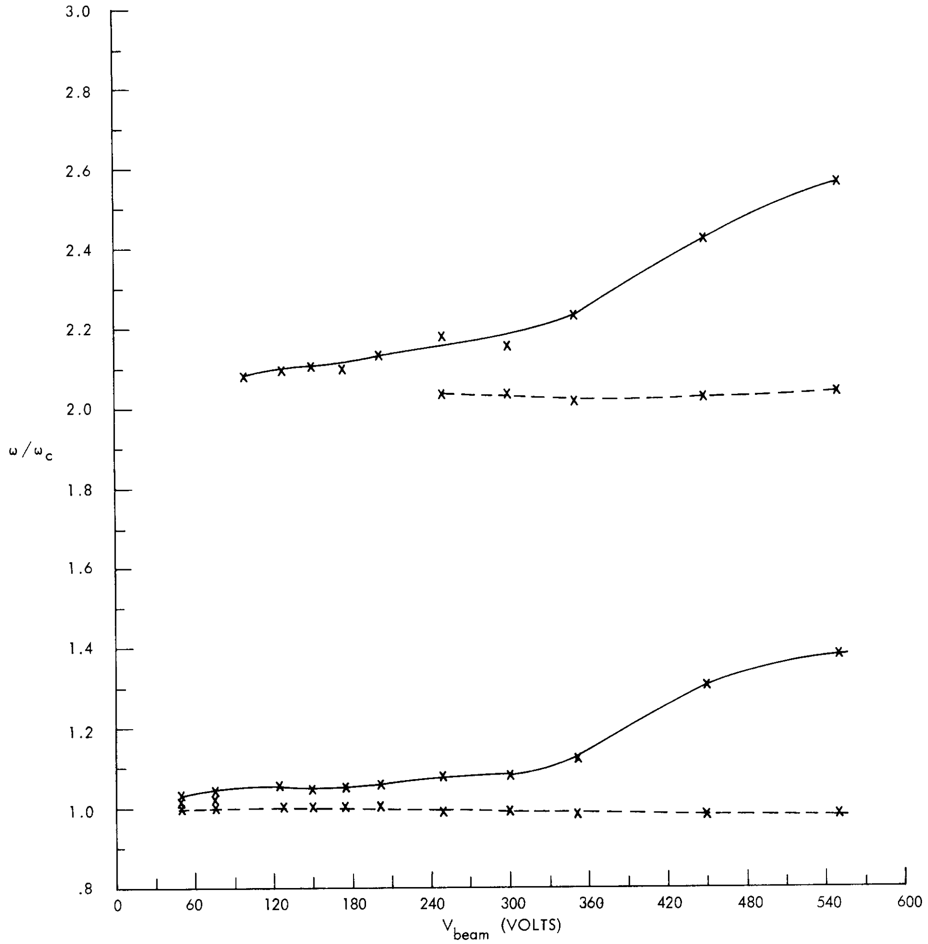

Fig. XI-16. Frequency of radiation peaks vs electron-beam voltage.

peak shifting from $n\omega_c$ toward a higher frequency as the plasma frequency is increased. The same comments regarding the similar behavior of the frequencies of the Bernstein modes for increasing plasma density apply here, too.

We now turn to the microwave scattering experiment. Since the warm plasma waves described by Bernstein[3] are longitudinal waves, E parallel to k, the electron density undergoes oscillations at the wave frequency, and microwave scattering from these oscillations should be possible. (References for the theory of microwave scattering have been given in a previous report.[9]) The experimental geometry for the scattering experiment is shown in Fig. XI-15b. The S-band waveguide was removed to allow the KA-band microwave horns access to the plasma. The oscillations in the plasma that are responsible for the radiation emitted into the waveguide were picked up by means of a strip-line antenna. This antenna was connected through a coaxial cable to the S-band radiometer tuned to 3000 Mc. Microwave power at a frequency of 34,700 Mc was incident on the plasma from one of the horns, and radiation scattered by the plasma was received by the second horn and detected by a radiometer tuned to 31,700 Mc. Thus any scattered radiation that was detected was shifted in frequency by 3000 Mc, the frequency of the oscillations in the plasma that were detected independently by the strip-line and the S-band radiometer. The magnetic field was varied, and the outputs of the S-band and KA-band radiometers were plotted simultaneously on two X-Y recorders. Figure XI-17 shows the results. The upper trace is the microwave power picked up directly from the plasma by the strip-line at 3000 Mc, and the three lower traces are the scattered microwave power for three values of incident microwave power. It can be seen that the peak in the scattered power disappears when no radiation is incident on the plasma, and that the peak appears at the same value of ω_c/ω as the large peak in the signal picked up directly from the plasma at 3000 Mc. (The nature of the small peak is not understood.) From these data, it seems clear that the peak in the microwave power received by the KA-band radiometer at 31,700 Mc is due to microwave scattering from the

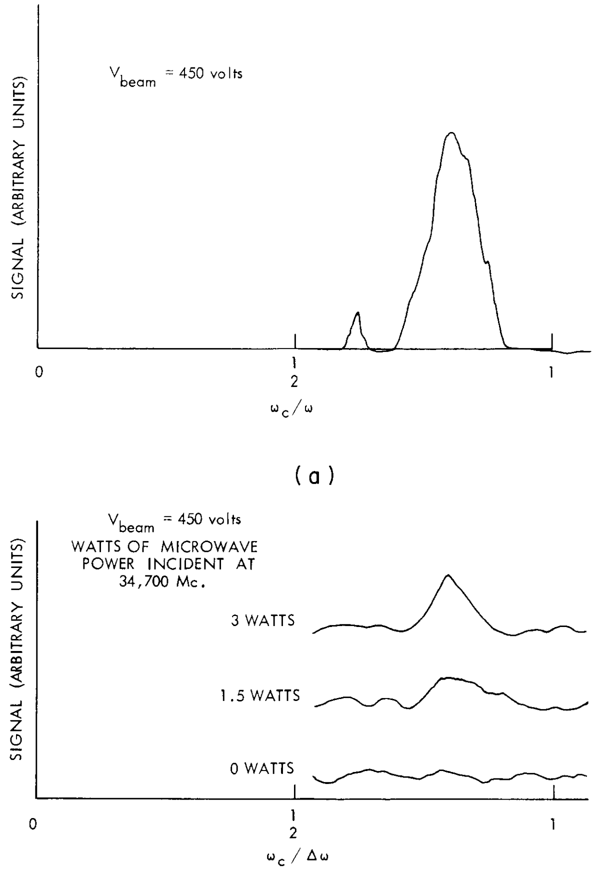

(a)

(b)

Fig. XI-17.

(a) Signal at 3000 Mc picked up from the plasma with strip-line antenna vs normalized magnetic field ($\omega = 2\pi \times 3000$ Mc).

(b) Scattered microwave power at 31,700 Mc vs normalized magnetic field. ($\Delta\omega$ = frequency shift between incident microwave frequency of 34,700 Mc and scattered microwave frequency of 31,700 Mc; $\Delta\omega = 2\pi \times 3000$ Mc.)

density oscillations associated with the waves that were observed directly at 3000 Mc. These waves seem to be the warm plasma waves described by Bernstein,[3] which become unstable, because of the presence of the beam electrons with a large component of velocity perpendicular to the magnetic field. No scattering was observed from the second harmonic, $\omega/\omega_c \gtrsim 2$, since the amplitude of the oscillations associated with it was much lower than the amplitude of the oscillations near the fundamental.

R. L. Kronquist

References

1. G. Bekefi, J. D. Coccoli, E. B. Hooper, Jr., and S. H. Buchsbaum, Phys. Rev. Letters 9, 6 (1962).
2. G. Landauer, Proc. Fifth International Conference on Ionization Phenomena in Gases, Munich, Germany, July 1961 (North-Holland Publishing Co., Amsterdam), Vol. 1, pp. 389-394.
3. I. B. Berstein, Phys. Rev. 109, 10-21 (1958).
4. E. Canobbio and R. Croci, Proc. Sixth International Conference on Ionization Phenomena in Gases, Paris, July 1963 (SERMA Publishing Co., Paris), Vol. 3, pp. 269-271.
5. F. W. Crawford and J. A. Tataronis, Seventh International Conference on Ionization Phenomena in Gases, Belgrade, 1965.
6. C. D. Lustig, W. D. McBee, and A. Kalisky, Sperry-Rand Research Center Report No. RR-645, Sudbury, Mass., January 1964; C. D. Lustig, Bull. Am. Phys. Soc. 9, 313 (1964).
7. S. Tanaka, K. Mitani, and H. Kubo, Institute of Plasma Physics Report No. 13, Nagoya University, Nagoya, Japan, July 1963; K. Mitani, H. Kubo, and S. Tanaka, J. Phys. Soc., Japan 19, 211 (1964); H. Kubo, K. Mitani, S. Tanaka, and Y. Terumichi, J. Phys. Soc. Japan 19, 221 (1964).
8. G. Bekefi and E. B. Hooper, Jr., Appl. Phys. Letters 4, 135 (1964).
9. R. L. Kronquist, Quarterly Progress Report No. 82, Research Laboratory of Electronics, M.I.T., July 15, 1966, p. 109.

E. NONLINEAR HARMONIC GENERATION AT PLASMA RESONANCE

The subject of this report is the generation of harmonics of an RF signal applied to a probe immersed in the sheath between the probe and the plasma. Harmonic generation is particularly copious at frequencies corresponding to resonances of the probe-plasma system. One such resonance, the geometrical resonance, is a manifestation of an oscillation of the sheath-plasma system.[1] This resonance frequency is near but below electron plasma frequency, ω_p. At geometrical resonance, sheath nonlinearities, in addition to generating harmonics, cause both the probe's RF admittance and the DC current collected by the probe to peak. These effects will be discussed here.

If a probe is inserted into a plasma, its RF admittance characteristic will show a resonance at a frequency somewhat below plasma frequency. This is attributed to a series resonance between the capacitive sheath and the inductive plasma. (A plasma acts as an inductance below plasma frequency, since the conduction current exceeds the displacement current for ω less than ω_p.) At series resonance, the electric fields in the sheath and plasma become large, and consequently large currents flow for a given voltage on the probe.

If the probe is now biased to collect DC current and an RF voltage is applied to the probe, more DC current is observed to flow than if there were no RF voltage. This effect can be explained approximately by considering the nonlinear current-voltage characteristic of the sheath surrounding the probe.

$$I = ne\left(\frac{kT_e}{2\pi m_e}\right)^{1/2} e^{-eV/kT_e}. \tag{1}$$

Here, n is the electron density, and V is the voltage drop across the sheath. When $V = V_o + V_1 \sin \omega t$,

$$I_{DC} = ne\left(\frac{kT}{2\pi m}\right)^{1/2} e^{-eV_o/kT} \left[\frac{1}{2\pi}\int_0^{2\pi} e^{-eV_1/kT \sin \omega t}\, d(\omega t)\right]. \tag{2}$$

The extra DC current that flows due to the RF voltage V_1 across the sheath is

$$\Delta I_{DC} = I_{DC}\left[I_o\left(\frac{eV_1}{kT}\right) - 1\right], \tag{3}$$

where I_o is the zero-order Bessel function of imaginary argument.

At series resonance, V_1 becomes large and ΔI_{DC} attains a maximum. It has been shown by Harp and Crawford that the incremental DC and RF admittance peak at the same frequency.[2]

If we now derive an equation for the instantaneous current by expanding the exponential in Eq. 3 and keep only the dominant contribution to each harmonic, we obtain[3]

$$\begin{aligned} I(t) &= I_{d_c}\left[1 + \left(\frac{eV_1}{kT}\right)\sin \omega t - \left(\frac{eV_1}{kT}\right)^2 \frac{\cos 2\omega t}{4} - \left(\frac{eV_1}{kT}\right)^3 \frac{\sin 3\omega t}{24} + \left(\frac{eV_1}{kT}\right)^4 \frac{\cos 4\omega t}{192} + \dots\right] \\ &= I_{DC} + I_1(\omega) + I_2(2\omega) + I_3(3\omega) + I_4(4\omega) + \dots . \end{aligned} \tag{4}$$

$I_1(\omega)$, $I_2(2\omega)$, etc. are the harmonics with which this report is concerned.

ΔI_{DC} in Eq. 3 is the time average of the harmonic current components. The RF admittance peak occurs because $I_1(\omega)$ attains a maximum at resonance. A schematic diagram of the experiment is shown in Fig. XI-18. The discharge, probe, and method of determining geometrical resonance were described in Quarterly Progress Report No. 79 (pages 95-98) and in a paper by Waletzko and Bekefi.[4]

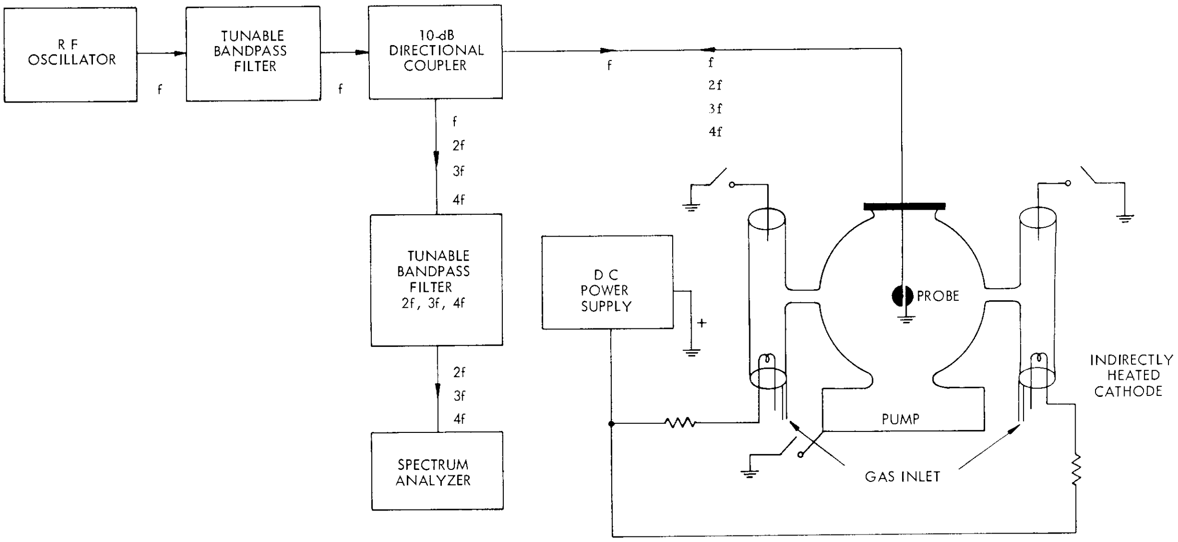

Fig. XI-18. Schematic diagram of the experiment.

Measurements of harmonic power were taken both on and off resonance. The amplitude of each harmonic peaked at resonance as expected. The harmonic power received as a function of the applied power for a fixed frequency and discharge conditions is shown in Fig. XI-19. These measurements were made on resonance.

It should be noted that V_1 is the voltage across the sheath and equals $V_{applied}$ only for ω much less than ω_p.[4] Nevertheless, for fixed discharge conditions and frequency, V_1 is proportional to $V_{applied}$ and the observed dependences shown in Fig. XI-19 are

Table XI-1. $\frac{I_4I_2}{I_3^2}$ for various runs.

	f_{inc} (MHz)	f_{res} (MHz)	$\frac{I_4I_2}{I_3^2}$
Approximate Theory			$\frac{3}{4}$
a)	50	50	2.2
b)	60	60	1.1
c)	60	60	2
d)	60	<60 Mc	1.1
e)	60	>60 Mc	8
f)	60	»60 Mc	16

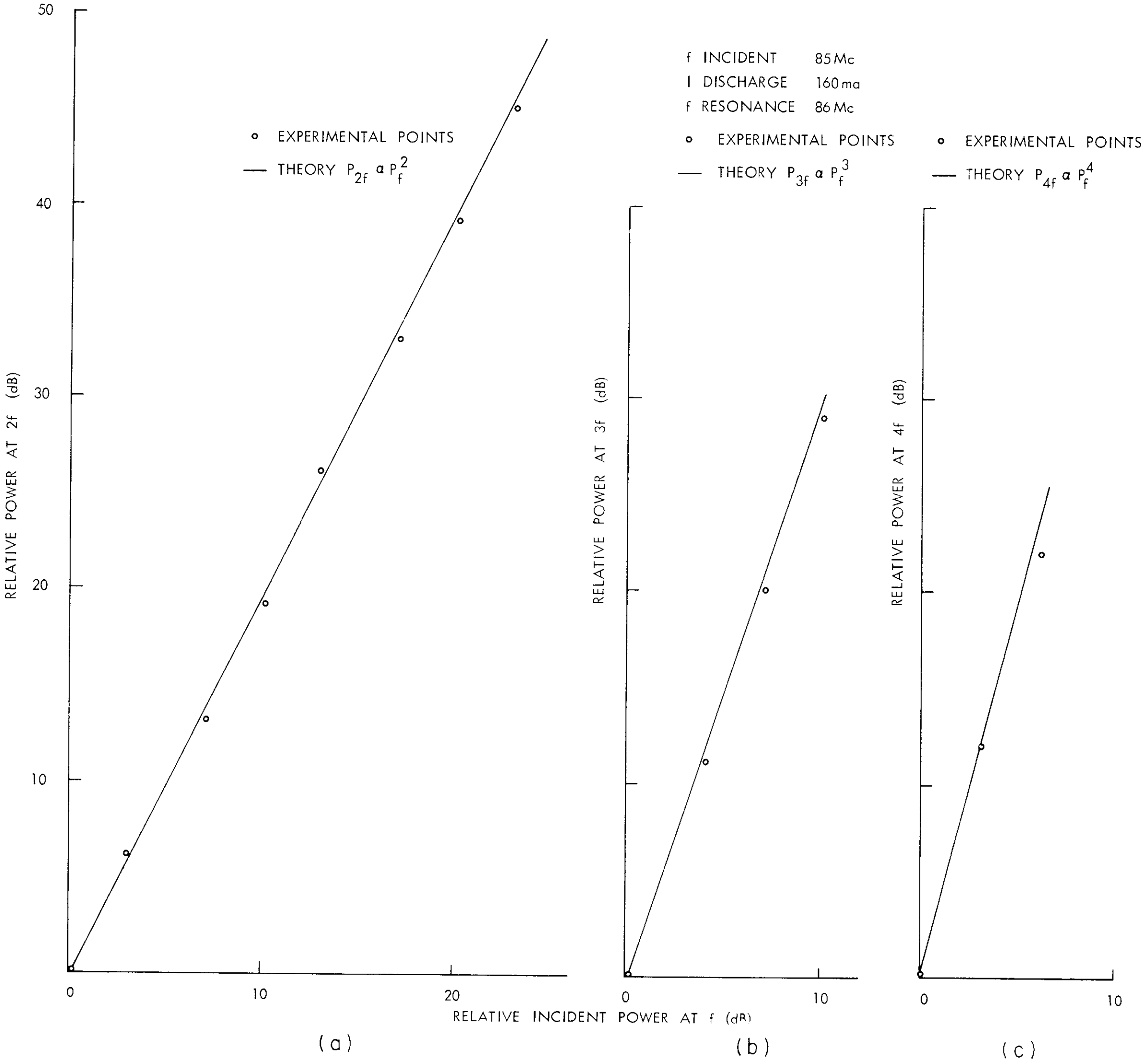

Fig. XI-19. (a) Relative power in the second harmonic vs relative fundamental power.
(b) Relative power in the third harmonic vs relative fundamental power.
(c) Relative power in the fourth harmonic vs relative fundamental power.

as expected from the approximate theory of Eq. 4.

We now wish to compare the relative magnitudes of observed harmonic emission with that predicted from Eq. 4. Since we do not know V_1,[5] we must look for a quantity independent of this parameter. From Eq. 4, one such quantity is $I_4I_2/I_3^2 = 3/4$. Table XI-1 shows the preliminary experimental results. Values a, b, c were taken at resonance. values d, e, f were taken off resonance, At f less than f-resonance, there is considerably more fourth harmonic than expected. The agreement for $f \sim f_{\text{resonance}}$ is fair. All measurements were made with a slotted-sphere antenna approximating a dipole.

The experiment is being refined in several ways. A monpole probe will be used so that a theory of harmonic amplitudes will be tractable. Since monopole fields are purely, radial, there is hope of solving the Vlasov equation for the monopole harmonic amplitudes. The voltage on the probe will be monitored so as to keep V_{applied} constant as the frequency is swept. Knowledge of the DC voltage and electron density in the sheath permits one to predict V_{RF} across the sheath in terms of V_{applied}. The DC bias on the probe will be varied to determine the effect of a varying sheath size on the harmonic generation.

A. J. Cohen

Footnotes and References

1. K. Takayama, H. Ikegami, and S. Miyasaki, Phys. Rev. Letters 5, 238 (1960); S. M. Levitskii and J. P. Shashurin, Sov. Phys. – Tech. Phys. 8, 319 (1963); R. Buckley, Proc. Roy. Soc. (London) A290, 186 (1966); D. Lepechinsky, A. Messian, and P. Rolland, Centre D'Etudes Nucleares de Saclay Rapport CEA-R 2945; J. A. Waletzko, "Radiofrequency Dipole Resonance Probe," Quarterly Progress Reports No. 79, Research Laboratory of Electronics, M.I.T., October 15, 1965, pp. 95-98; No. 80, January 15, 1966, pp. 103-108; R. S. Harp and F. W. Crawford J. Apl. Phys. 35, 3436-3446 (1964).
2. R. S. Harp and F. W. Crawford, J. Appl, Phys. 35, 3444 (1964).
3. Equation 4 is valid for $eV_1/kT \leq 1$, This criterion is not necessarily satisfied at resonance, since V_1 can become very large there.
4. J. A. Waletzko and G. Bekefi (submitted to Journal of Radio Science).
5. $V(n\omega) = K_n[V_1(\omega)]^n$ theory. The aim of the theory is to calculate the harmonic conversion efficiency constant K_n. But V_1 is not known experimentally. $V_1 = f(\omega)\, V_{\text{applied}}$, where $f(\omega)$ is determined by the resonance (see Buckley, Lepechinsky et al.[1]) V_{applied} is not yet known, only V_{output} and the probe impedance at frequency ω are known. V_{applied} cannot be simply determined by transmission-line theory because the oscillator output is a strong function of its loading. For example, at resonance the probe impedance is small so V_{applied} is small but $f(\omega)$ is large. Off resonance, the impedance is high, V_{applied} is large, and although $f(\omega)$ is small, V_1 can be large. Only if V_{applied} is held constant can the effect of any resonances on the harmonic generation be clearly observed.

F. LASER BREAKDOWN EXPERIMENT

This report presents a further analysis of the laser breakdown experiment.[1,2]

1. Absorption Coefficient

The absorption coefficient of the plasma for the light of the HeNe gas laser can be readily calculated from the transmission of the laser beam through the plasma and the radius of the cylindrical spark. The diameter of the laser beam is 2 mm and the diameter of the plasma is greater than 2 mm from 110 nsec on, after the beginning of the Gaunt pulse.

The first experimental point of the transmission curve is at 130 nsec. Figure XI-20 shows the arrangement that was adopted. The volume, V_e, of the plasma crossed at 90° by the gas laser beam is limited by the volume of the two cylinders, and for its lateral surface it has the surface of the gas laser beam itself.

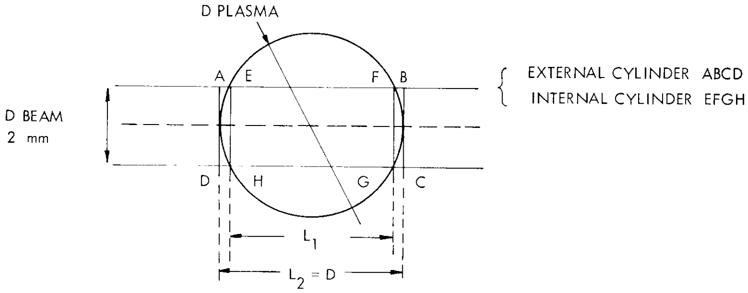

Fig. XI-20. Model for calculating the absorption coefficient of the plasma for the light of the gas laser (6328 Å).

$$\text{Vol}_{\text{external}} > \text{Vol}_{\text{plasma crossed}} > \text{Vol}_{\text{internal}}.$$

Thus, for a given diameter of the plasma, the true absorption coefficient will be between the values α_1 and α_2, satisfying the equations

$$T_r = e^{-\alpha_1 L_1} \qquad T_r = e^{-\alpha_2 L_2},$$

where L_1 and L_2 are the lengths of the two cylinders, and T_r is the transmission, at time t, of the gas laser beam through the plasma. Applying this technique to the points and extreme values of the error bars of T_r, we obtained the absorption coefficient at 6328 Å (Fig. XI-21). For times between 130 nsec and 600 nsec, the

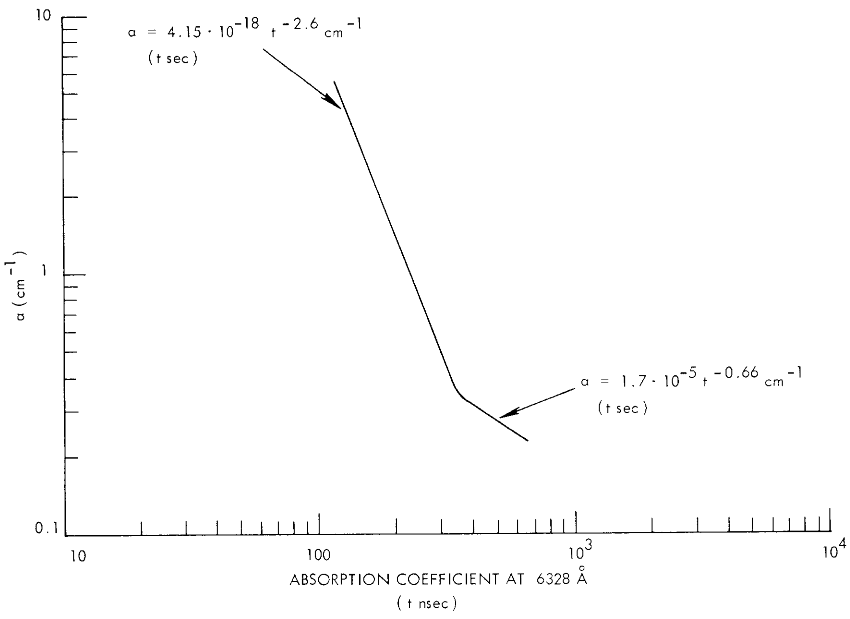

Fig. XI-21. Absorption coefficient at 6328 Å.

absorption coefficient drops from 4 cm^{-1} to ~0.25 cm^{-1}. At approximately 300 nsec, the behavior of α changes from

$$\alpha = 4.15 \times 10^{-18}\, t^{-2.62}\ \text{cm}^{-1}\ (\text{t sec}) \tag{1}$$

to

$$\alpha = 1.7 \times 10^{-5}\, t^{-.66}\ \text{cm}^{-1}\ (\text{t sec}). \tag{2}$$

Since α and R versus time are known, the optical thickness of the plasma $\tau = 2\alpha R$ can be obtained immediately. The approximation that is used is very good, within the uncertainty of experimental error. The change in slope of absorption coefficient occurs when the plasma emits the axial and radial shock waves.

2. Density

The measured electron density, recording the spreading of the gas laser beam, caused by the lens effect of the plasma, is shown in Fig. XI-22. The density slope changes when the subsonic regime is reached.

It has to be kept in mind that, for every time, the density measured by this method is not the average density across the circular section of the plasma. The density has a profile across the section and it is the density corresponding

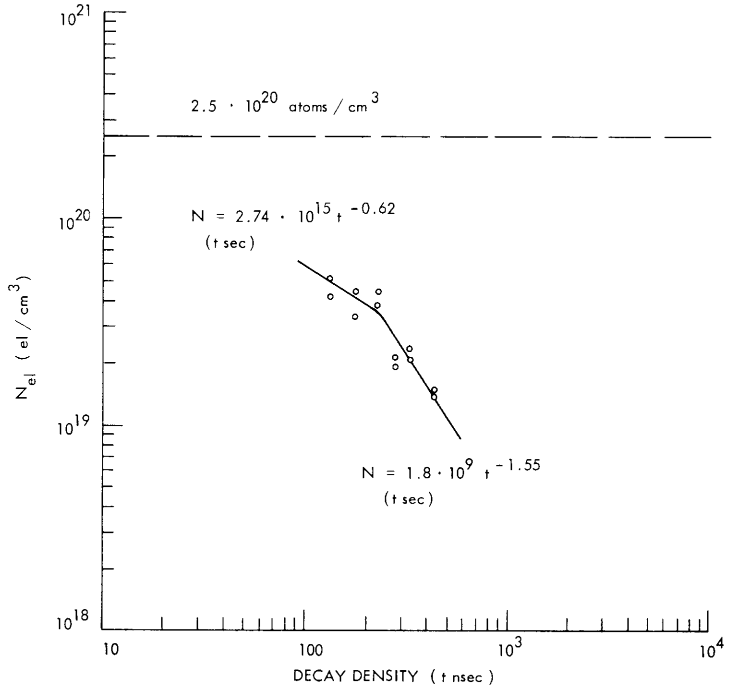

Fig. XI-22. Electron density measurement.

to the central higher part of this profile that gives the maximum angular scattering. The lens and the adjustable diaphragm detect this maximum solid angle of scattering, and so the measured density is not the average value across the circular section of the plasma. The density behavior from 100 nsec to approximately 250 nsec is

$$N = 2.74 \times 10^{15}\, t^{-.62}\, \frac{\text{electrons}}{\text{cm}^3}. \tag{3}$$

From ~250 nsec to ~600 nsec the density (always measured in the central part of the plasma) is

$$N = 1.8 \times 10^{9}\, t^{-1.55}\, \frac{\text{electrons}}{\text{cm}^3} \tag{4}$$

The profile of the density will be obtained from the "knee curves"[2] that describe the transmission of the gas laser beam through the plasma.

By subtracting the transmission between two consecutive diaphragm apertures and correcting with the known absorption coefficient, averaged through the plasma, a scattering profile for the gas laser beam will be obtained. The profile of the refraction index through the plasma that modifies the initial gas laser beam profile in the scattered profile will thus be obtained for every time. Further work is in progress on this point.

3. Shock Velocity

From previous work,[4] which has shown the behavior of the longitudinal and radial expansion of the plasma, a full description of the size of the plasma and of the shock wave emission can be obtained.[5,6] Between 50 nsec and 200 nsec the growth of the radius of the plasma from the initial value is

$$R = 1.7 \times 10^{6}\, t^{1.04} \text{ cm (t sec).} \tag{5}$$

When the shock wave starts to be emitted, the radius growth slows down and the radius is (from 300 nsec to 32 μsec)

$$R = 7.4 \times 10^{-1}\, t^{.09} \text{ cm (t sec).} \tag{6}$$

The shock radius from ~500 nsec to 5 μsec is

$$R = 2.29 \times 10^{2}\, t^{.46} \text{ cm (t sec).} \tag{7}$$

Figure XI-4 shows the behavior of the velocity of the plasma radius and of the shock. The plasma radius shock slows down to the velocity of sound in the unperturbed gas, and so do the axial velocities.

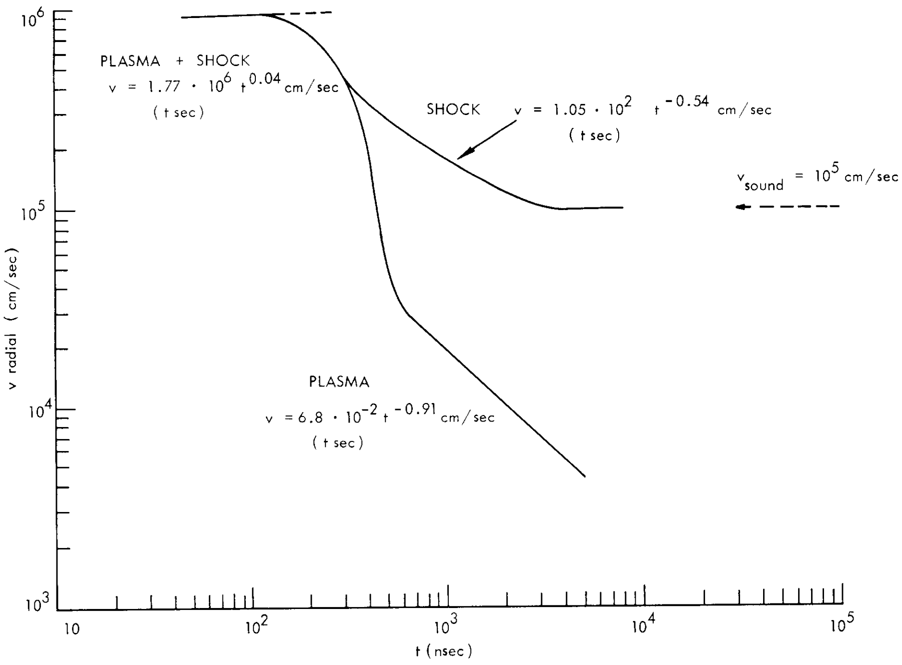

Fig. XI-23. Plasma radial velocity.

$$V_{\text{sound}} = \sqrt{\frac{\gamma p}{\rho}}. \tag{8}$$

That is, for $\gamma = 1.66$ and $p = 10.25\ \frac{\text{kg}}{\text{cm}^2}$, $\rho = 1.67 \times 10^{-3}\ \frac{\text{gr}}{\text{cm}^3}$, and $V = 10^5\ \frac{\text{cm}}{\text{sec}}$. The shoulder plasma dragged by the radial shock wave is found up to a radius $R = 5$ mm ($t = 8$ μsec).[7,8] The longitudinal growth of the plasma toward the ruby beam is shown in Fig. XI-24. Figure XI-25 gives the velocity behavior in the same direction. Figures XI-26 and XI-27 give the longitudinal growth and velocity in the direction of the beam. In the direction toward the ruby beam the growth in plasma length from the initial size of 4.5 mm is

$$L = 80\ t^{.41}\ \text{cm (t sec)} \tag{9}$$

for times from 30 nsec to the beginning of the separation of the shock wave from the plasma (500 nsec). The shock, measured between 500 nsec and 10 μsec is given by

$$L = 1.5 \times 10^3\ t^{.61}\ \text{cm (t sec)}. \tag{10}$$

The plasma slows down and its growth in length, measured between 500 nsec and 25 μsec, is

$$L = 5.1 \times 10^{-1}\ t^{.068}\ \text{cm (t sec)}. \tag{11}$$

The motion of the exploding front against the ruby is in good agreement with Taylor's blast-wave theory.[5,6] The front position, according to this theory, is given by

$$L = \left(\frac{E}{\rho}\right)^{.2} t^{.4}\ \text{cm (t sec)}, \tag{12}$$

where E is the energy in the explosion, and ρ is the mass density. For times between 30 μsec and 500 μsec, when the shock front is still inside the plasma, introducing into (12) the values $E = 1.8$ joules (which, as we shall see, is a reasonable estimate for the energy left in the plasma after the ionization) and $\rho = 1.67 \times 10^{-3}\ \frac{\text{gr}}{\text{cm}^3}$, we find

$$L = 101\ t^{.4}\ \text{cm (t sec)},$$

which agrees with (9), within 20 per cent. The behavior in the direction following the ruby beam, is quite different. The plasma front before the separation of the shock (400 nsec) is

$$L = 2.59 \times 10^6\ t^{1.14}\ \text{cm (t sec)}. \tag{13}$$

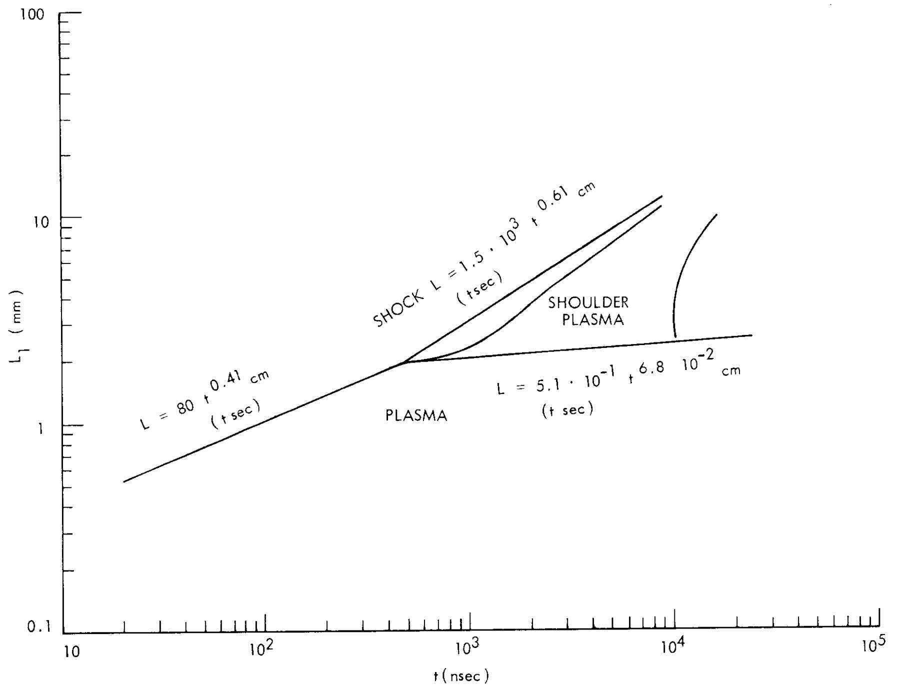

Fig. XI-24. Axial growth toward the ruby.

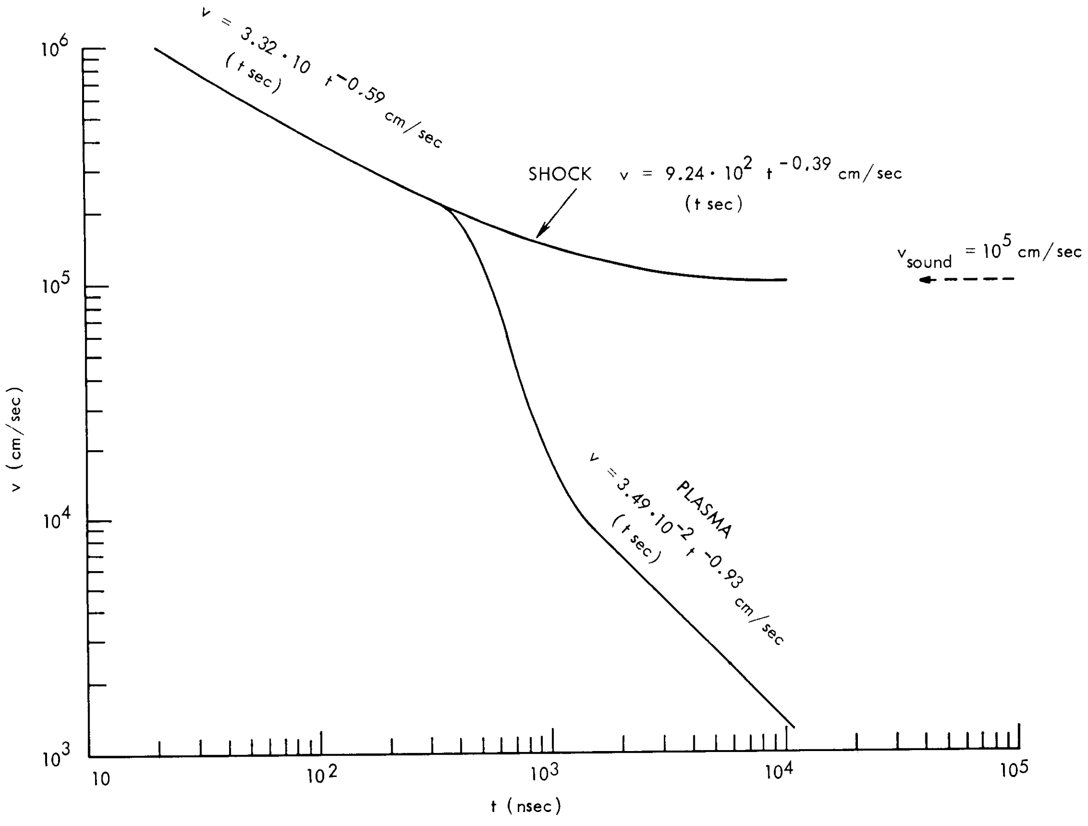

Fig. XI-25. Axial velocity toward the ruby.

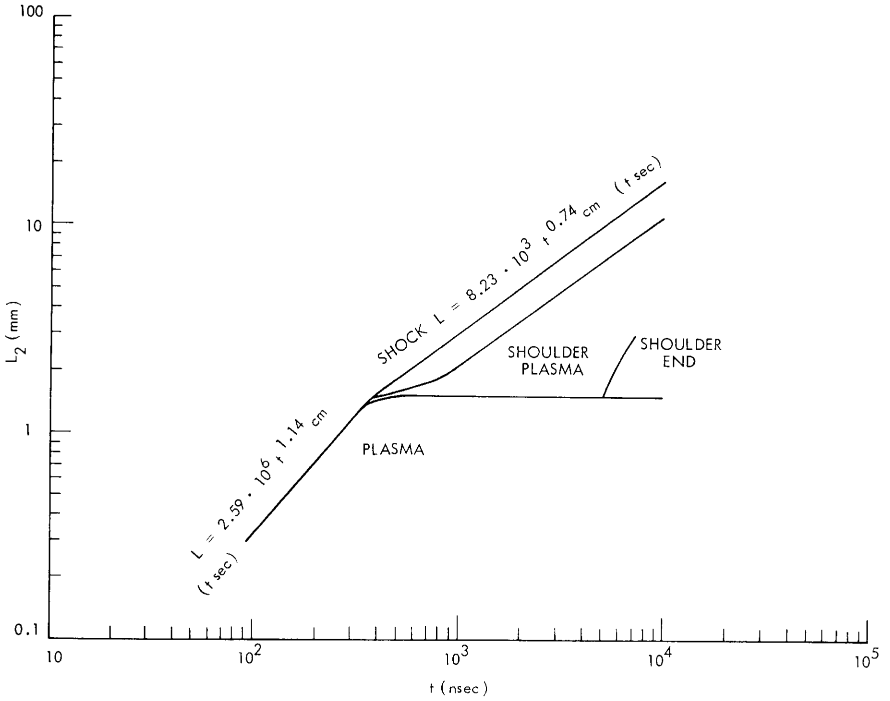

Fig. XI-26. Axial growth in the direction of the ruby.

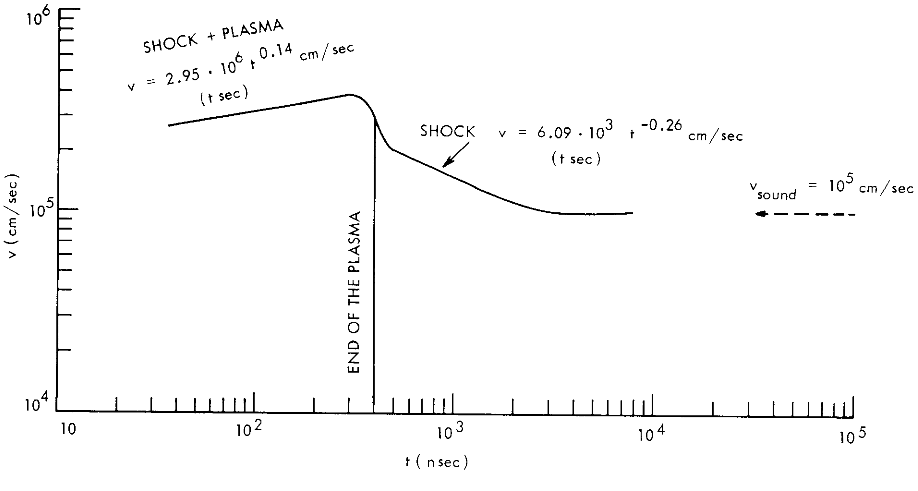

Fig. XI-27. Axial velocity in the direction of the ruby.

After the beginning of the separation, the shock is given by

$$L = 8.23 \times 10^3 \, t^{.74} \text{ cm (t sec).} \tag{14}$$

The plasma, after the beginning of the separation from the shock, slows greatly and does not expand farther beyond 1.4 mm than the initial position. This confirms the fact that the plasma explodes mainly towards the focussing lens. Under the assumption that the plasma has the shape of a cylinder, the volume is immediately found from the radius and length. Figures XI-28 and XI-29 give the volume and the volume velocity of the plasma. The volume velocity is growing before 200 nsec. More detailed work is in the course of interpretation of the axial expansion data in the direction of the ruby beam.

4. Temperature Measurement

The measurement of the average temperature of the plasma during the afterglow between 130 nsec and 600 nsec is made with the experimental arrangement previously reported.[2] To avoid directional effects on the transmission of the sharp interference filter I with respect to the emission beams coming from the plasma through the lens G, the diaphragm H was kept at a relatively small diameter f/22, that is, 16.35 mm; the solid angle from which the points of the plasma (distant 183 cm from the diaphragm) see the aperture of the diaphragm itself is $\Delta\Omega = 6.26 \times 10^{-5}$ steradian. The gas laser beam, when the plasma is not present, passes through the aperture of the diaphragm. The method of measurement of the temperature consists in calibrating, with the DC signal of the gas laser, the emission signal of the plasma, which the two interference filters in cascade receive in a resulting 10 Å bandwidth centered at 6328 Å; this wavelength is far from the radiation lines of Helium (the nearest lines are 5876 Å and 6678 Å) and the emission of the plasma at 6328 Å is entirely due to Bremsstrahlung. When the plasma is produced, no gas laser is on, and the photomultiplier tube receives the emission of the plasma through the interference filters D and I, the sharp cutoff filter B, and the polarizer C. Many emission curves are taken in the same situation to keep account of the nonexact repetitiveness of the plasma (Fig. XI-30). Then, when no plasma is present, the gas laser is put into operation and, in this way, a steady-state signal

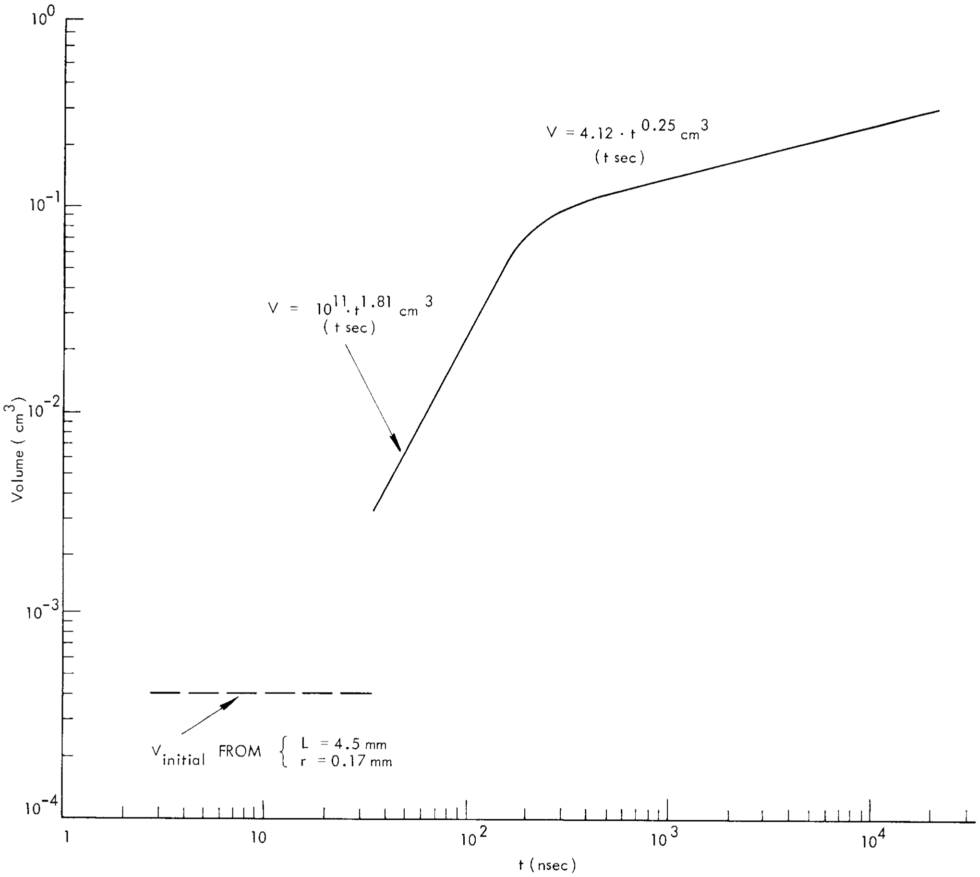

Fig. XI-28. Volume of the plasma.

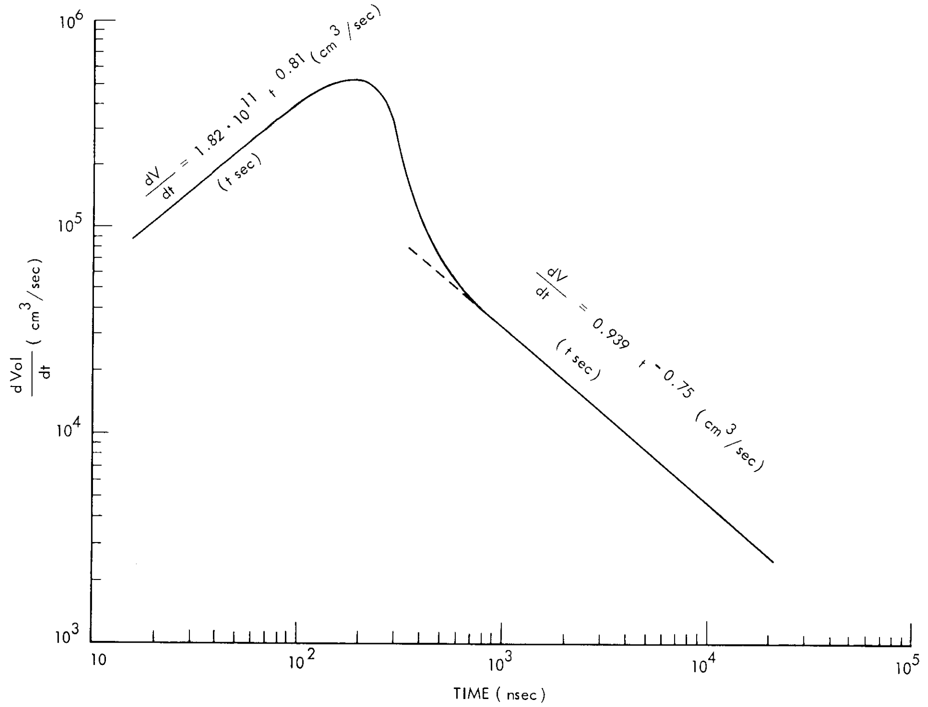

Fig. XI-29. Volume velocity of the plasma.

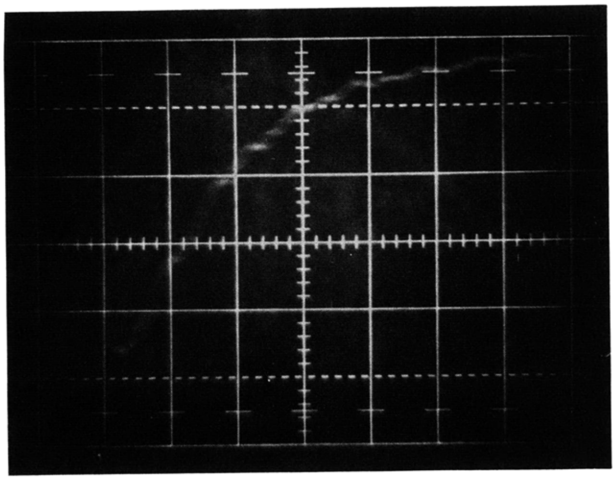

Fig. XI-30. Plasma emission (f/22) for measurement of temperature. Scales: Vertical, 5 mV/cm; horizontal 100 nsec/cm.

is received by the detector that works always in its linear regime. A Spectra-Physics Type 401B calorimetric power meter is then used for measuring the power of the gas laser in two points: before entering the plasma chamber (immediately after diaphragm A), and before the interference filter I. In this way, the gas laser DC signal is calibrated in power. We make use of the following notation.

$\Gamma(t)$: the power (varying in time) that the diaphragm H receives from the plasma per unit radian frequency.

$$\Gamma = \frac{\text{erg}}{\left(\frac{\text{rad}}{\text{sec}}\right)\text{sec}}$$

$\xi_{\substack{\text{sharp}\\\text{cut}}}$: the transmission of the sharp cutoff filter at 6328 Å = 90%.

$\xi_{\text{IF}}\ \Delta\omega_{\text{IF}}$: the product of the bandwidth of the cascade of the two interference filters for the average transmission of the cascade itself

$$\xi_{\text{IF}}\ \Delta\omega_{\text{IF}} = 8.4 \times 10^{11}\ \frac{\text{rad}}{\text{sec}}$$

$$\Delta\omega_{\text{IF}} = 7.26 \times 10^{12}\ \frac{\text{rad}}{\text{sec}}.$$

ξ_{pol}: the transmission of the polarizer for unpolarized light = 34%.

ξ_{silv}: the reflectivity of each silvered mirror, E and F, for light at 6328 Å (80%).

ξ_{PM}: the efficiency of the photomultiplier at 6328 Å.

L: the load of the photomultiplier tube (38Ω).

Then we can write

$$\Gamma(t)\, \xi_{\substack{\text{sharp}\\ \text{cut}}}\, \xi_{IF}\, \Delta\omega_{IF}\, \xi_{pol}\, \xi^2_{silv}\, \xi_{PM}\, L = V^{(t)}_{\text{plasma emission}}, \tag{15}$$

where $V^{(t)}_{\text{plasma emission}}$ is the signal from the plasma (see Fig. XI-30) given by the photomultiplier. The transmittance of the lens and the quartz windows is not included. Equation 15 is the emission equation. We then introduce the following notation.

$P_L = \dfrac{\text{erg}}{\left(\frac{\text{rad}}{\text{sec}}\right)\text{sec}}$, the gas-laser power entering the plasma chamber during the calibration.

$\xi_{POL.\,GL}$: the transmittance of the polarizer for the polarized and parallel gas laser light = 70%.

$\xi_{\substack{IF\ PEAK\\ SHARP}}$: the peak transmittance of the interference filter, I, for the gas laser light at 6328 Å = 50%.

$\xi_{\substack{IF\ PEAK\\ NONSHARP}}$: the peak transmittance of the IF filter, D (20 Å bandwidth).

$\Delta\omega_L$: the bandwidth of the gas-laser light. (Keep in mind that an attenuator neutral filter with transmittance ξ_{ATT} = 18.5% was put in front of the photomultiplier tube during the calibration to have the tube working in the linear regime.)

Then we can calibrate the optical system.

$$P_L\, \xi_{\substack{\text{sharp}\\ \text{cut}}}\, \xi_{POL.\,GL}\, \xi_{\substack{IF\ PEAK\\ SHARP}}\, \xi_{\substack{IF\ PEAK\\ NONSHARP}}\, \Delta\omega_L\, \xi^2_{silv}\, \xi_{ATT}\, \xi_{PM}\, L = V_{steady}, \tag{16}$$

where V_{steady} is the signal (in volts) from the DC gas laser on the oscilloscope during the calibration. Indicating, with M, the power of the gas-laser beam, measured in milliwatts by the calorimeter before the interference filter, I, we can write

$$P_L\, \xi_{\substack{SHARP\\ CUT}}\, \xi_{POL.\,GL}\, \xi_{\substack{IF\ PEAK\\ NONSHARP}}\, \Delta\omega_L\, \xi^2_{silv} = M. \tag{17}$$

With the use of Eq. 17, Eq. 16 becomes

$$M\, \xi_{\substack{IF\ PEAK\\ SHARP}}\, \xi_{ATT}\, \xi_{PM}\, L = V_{steady}. \tag{18}$$

Calling $\frac{V^{(t)}_{\text{emission}}}{V_{\text{steady}}} = K(t)$ and using Eq. 18, we can rewrite Eq. 15 as follows:

$$\Gamma(t)\, \xi_{\substack{\text{SHARP}\\ \text{CUT}}}\, \xi_{\text{IF}}\, \Delta\omega_{\text{IF}}\, \xi_{\text{POL}}\, \xi^{2}_{\text{silv}}\, \xi_{\text{PM}}\, L = K(t)\, M\, \xi_{\substack{\text{IF PEAK}\\ \text{SHARP}}}\, \xi_{\text{ATT}}\, \xi_{\text{PM}}\, L$$

from which we get

$$\Gamma(t) = K(t)\, \frac{\xi_{\substack{\text{IF PEAK}\\ \text{SHARP}}}\, \xi_{\text{ATT}}}{\xi_{\substack{\text{SHARP}\\ \text{CUT}}}\, \xi_{\text{IF}}\, \Delta\omega_{\text{IF}}\, \xi_{\text{POL}}\, \xi^{2}_{\text{silv}}} \cdot M$$

$$\Gamma(t) = K(t)\, M\, 5.6 \times 10^{-13}.$$

The presence of the quartz window of the plasma chamber and of a quartz slab used to set the gas laser beam in position bring the factor 5.6×10^{-13} to the value 6.4×10^{-13}. We finally obtain

$$\Gamma(t) = K(t)\, M\, 6.4 \times 10^{-13}. \tag{19}$$

By calibrating with the gas laser at a value $V_{\text{steady}} = 20$ mV on the oscilloscope, a power $M = 0.078$ mW was measured with the calorimeter. Equation 19 then becomes

$$\Gamma(t) = K(t)\, 5 \times 10^{-10}, \tag{20}$$

where $\Gamma(t)$ is measured in $\frac{\text{erg}}{\left(\frac{\text{rad}}{\text{sec}}\right)\text{sec}}$, and $K(t)$ is a pure number directly obtained from the emission signal of the plasma. The problem now is to relate the emission power, per unit radian frequency, $\Gamma(t)$, collected by the diaphragm H to the source function S_ω of the plasma, that is, the well-known Planck function

$$S_\omega = \frac{\hbar\omega^3}{4\pi^3 c^2}\, \frac{1}{e^{\left(\frac{\hbar\omega}{kT}\right)} - 1}\, \frac{\text{erg}}{\left(\frac{\text{rad}}{\text{sec}}\right)\text{sterad cm}^2\text{ sec}}. \tag{21}$$

Figure XI-31 shows the model for calculating $\Gamma(t)$, that is, the radiation power per unit frequency received by diaphragm H from the plasma cylinder situated 183 cm away. The angle ψ is practically zero. The radiation received by the diaphragm H and emitted by the elementary surface centered in P comes

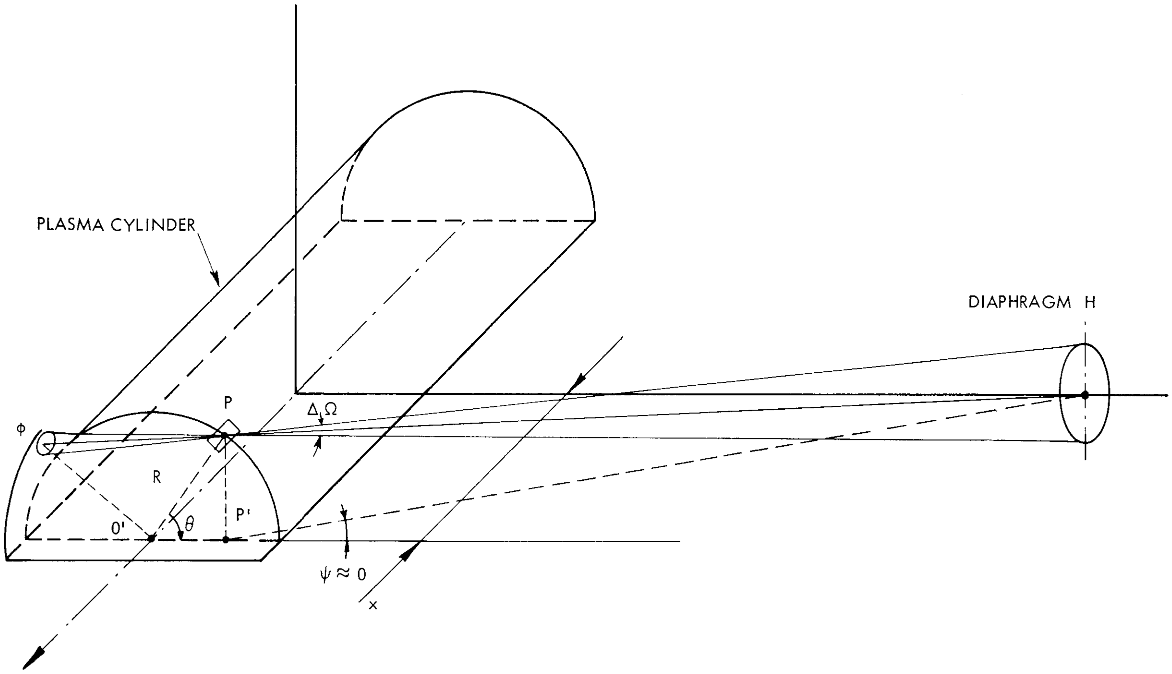

Fig. XI-31. Plasma model for calculating the radiation received from diaphragm H.

from the cone of the plasma with vertex in P and base in Q that sees the aperture of H.

$$\Gamma(t) = \Delta\Omega S_\omega LR \int_{-\pi/2}^{\pi/2} \left[1-e^{-2R\alpha \cos\theta}\right] \cos\theta \, d\theta, \tag{22}$$

where $\Delta\Omega$ is the solid angle through which P sees the diaphragm H, L is the length of the plasma (cm) at time t, R is the radius of the plasma at time t, that is,

$$\Gamma(t) = \Delta\Omega S_\omega LR \left[2-I(z)\right],$$

where

$$I(z) = \int_{-\pi/2}^{\pi/2} e^{z\cos\theta} \cos\theta \, d\theta$$

and $z = -2\alpha R$.

By developing the exponential in a series of Bessel functions

$$e^{z\cos\theta} = I_0(z) + 2 \sum_{K=1}^{\infty} I_K(z) \cos(K\theta)$$

the integral is solved and becomes

$$I = 2I_o(z) + \pi I_1(z) + 4 \sum_{n=1}^{\infty} \frac{I_{2n}(z)(-1)^{n+1}}{4n^2 - 1}. \tag{23}$$

Equation 22 then becomes

$$\Gamma(t) = \Delta\Omega S_\omega(t)\ L(t)\ R(t)\ 2\left[1 - I_o(z) - \frac{\pi}{2} I_1(z) - 2 \sum_{n=1}^{\infty} \frac{I_{2n}(z)(-1)^{n+1}}{4n^2 - 1}\right],$$

where z is the reciprocal of the optical thickness of the plasma whose behavior, in time, is known (Fig. XI-32). Calling f(z) the quantity enclosed in square brackets, we have

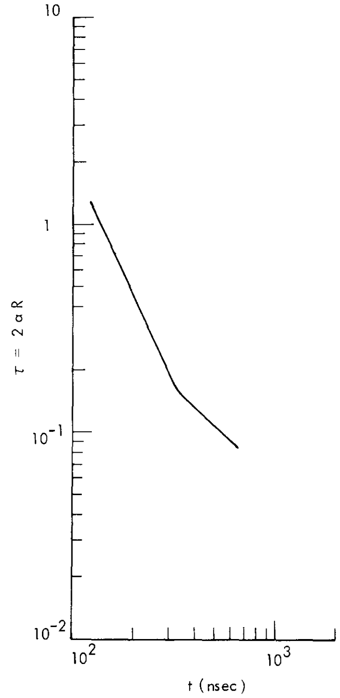

Fig. XI-32. Radial plasma optical thickness.

$$\Gamma(t) = \Delta\Omega S_\omega(t)\ L(t)\ R(t)\ 2f[z(t)]. \tag{24}$$

Developing the Bessel functions in series

$$I_r(z) = \left(\frac{z}{2}\right)^r \sum_{K=0}^{\infty} \frac{\left(\frac{z^2}{4}\right)^K}{K!\ \Gamma(r+K+1)},$$

changing $-z$ in τ (optical thickness of the plasma), we get

$$f(z) = \phi(\tau) = \tau(0.785) - \tau^2(0.333) + \tau^3(9.8\times 10^{-2})$$
$$- \tau^4(2.22\times 10^{-2}) + \tau^5(4.08\times 10^{-3}) - \tau^6(6.35\ 10^{-4}). \tag{25a}$$

Figure XI-33 is a plot of f(z); the straight line is the approximated f(z) obtained by developing the exponential $e^{z \cos \theta}$ as $1 + z \cos \theta$ and neglecting higher order terms. The corresponding $\phi(\tau)$ is just the first-order term of f(z) complete.

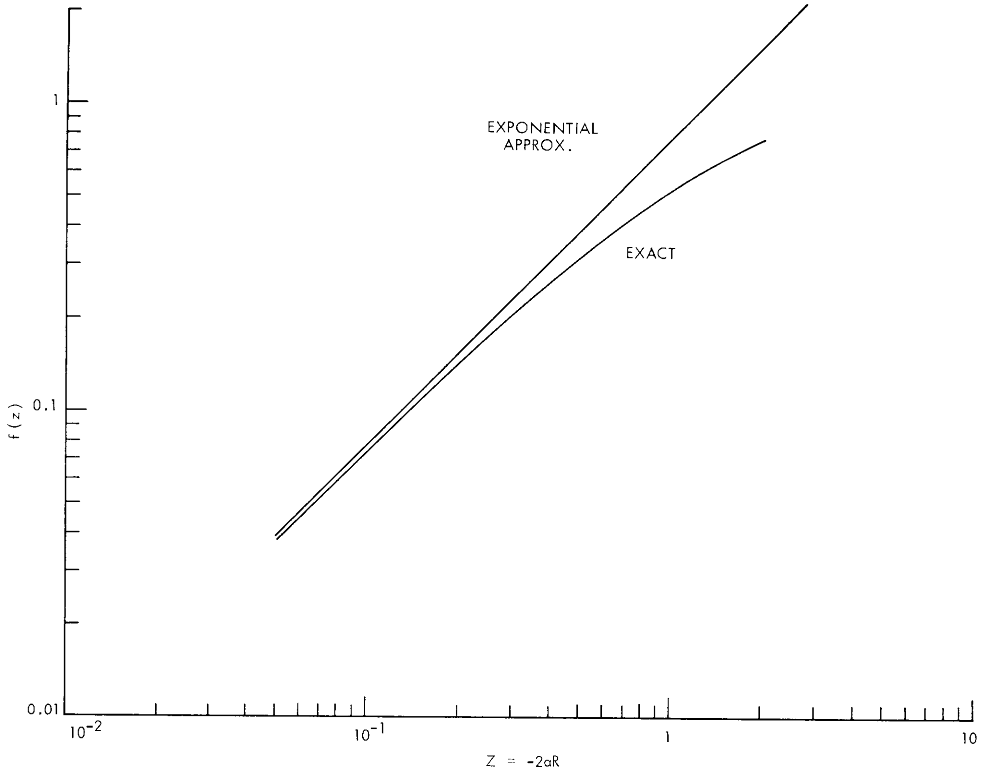

Fig. XI-33. Integrated absorptivity.

The source function S_ω is now readily known. Reading from three emission curves like the one in Fig. XI-30 (for calculating the error bars), the values of K(t) versus time, Γ(t) is known immediately from (20) and (24). Remembering that $2\Delta\Omega = 1.25\times 10^{-4}$ steradian, we get

$$S_\omega(t) = 4 \times 10^{-6} \frac{K(t)}{L(t)\ R(t)\ f[z(t)]} \text{ (CGS System).} \tag{25b}$$

Introducing in (25b) the known quantities K(t), L(t), R(t) $f[z(t)] = \phi[\tau(t)]$, we finally get $S_\omega(t)$ (Fig. XI-31). From $S_\omega(t)$ known at the frequency of the HeNe gas-laser line at

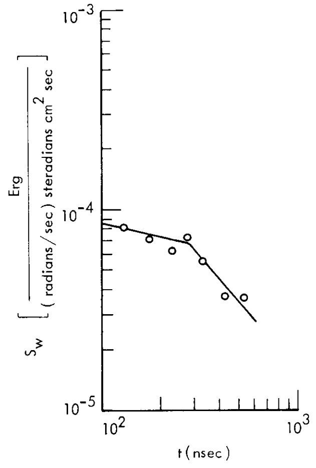

Fig. XI-34. Planck function $S_\omega = \frac{\hbar\omega^3}{4\pi^3 c^2} \frac{1}{e^{\frac{\hbar\omega}{kT}} - 1}$.

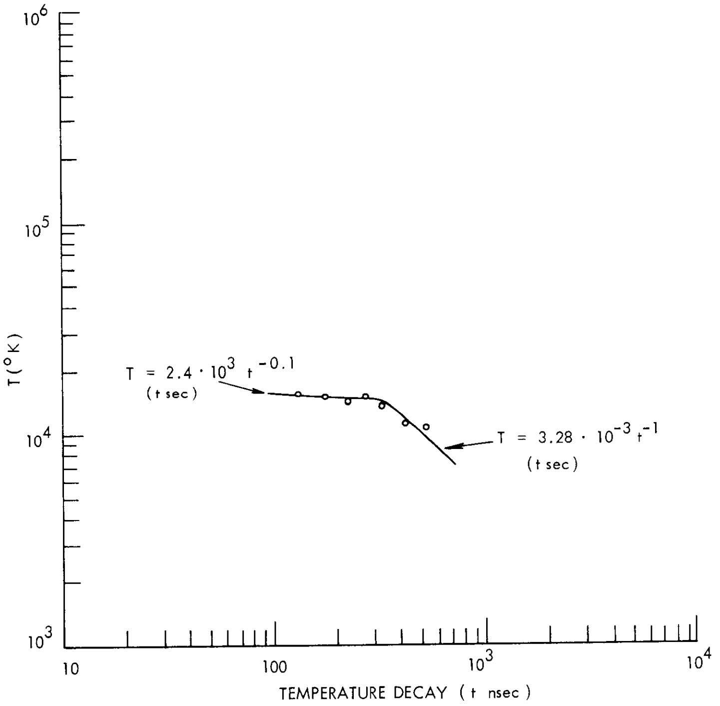

Fig. XI-35. Temperature decay.

$\omega = 2.975 \times 10^{15}$ rad/sec, the temperature is immediately obtained (Fig. XI-35). The decay is practically isothermal up to the time when the shock wave in the radial direction starts to be emitted; the decay then goes as t^{-1} up to ~600 nsec.

5. Temperature Density Dependence

Plotting the density (in the central part of the plasma) against the temperature, we find (Fig. XI-36) that, for times larger than 300 nsec, the temperature goes as $T \equiv N^{2/3}$,

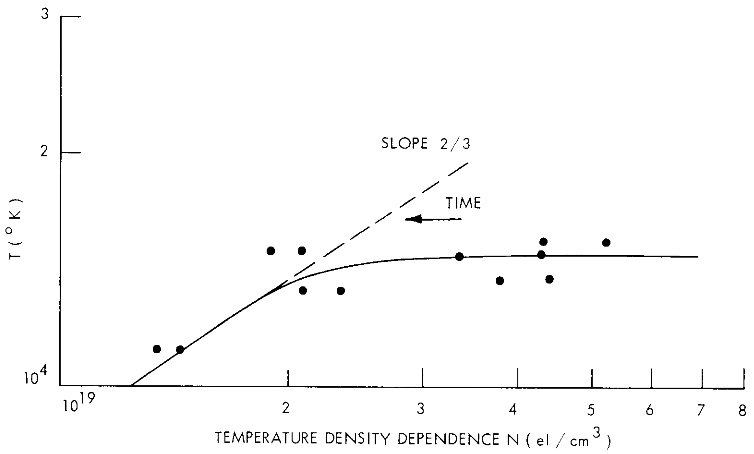

Fig. XI-36. Density vs temperature.

that is, the dependence is adiabatic during the shock wave emission.[9] This fact can be shown better if we calculate the entropy per electron from the Sackur-Tetrode formula for a perfect gas.[10]

$$\frac{S}{N_{\text{total}}} = k \ln \left[\frac{1}{N} e \left(\frac{2\pi M}{h^2} \right)^{3/2} (kT)^{3/2} \right] + \frac{3}{2} k \tag{26}$$

where

h is Planck's constant
M is the mass of the electron
k is Boltzmann's constant
N is the density of the electrons
N_{total} is the total number of electrons in the plasma
e is the base of natural logarithms.

The function $\frac{S}{N_{\text{total}}}$ is plotted against the time in Fig. XI-37, in which it is clearly seen that the entropy per single electron, which before the shock emission is

$$\frac{S}{N_{\text{total}}} = 0.6 \times 10^{-23} \ln (t) + \text{constant}, \tag{27}$$

changes to a constant value, when the radial shock starts to come out from the plasma. This change of slope is found also in the density; a possible explanation is that the plasma while exploding and not starting to emit the shock wave is strongly shock-ionizing the gas met by its explosive front. When the shock starts to emerge from the plasma surface, the expansion is strongly slowed down and the shock ionization stops and does not compensate any more for the recombination loss; the dependence on time of the density then drops from $t^{-.62}$ to $t^{-1.55}$. The fact that the measured density corresponds to the central high part of the density profile and so is not the average density through the plasma section is confirmed by the fact that the measured values of the absorption coefficient over the square of the density a/N^2 are lower by a factor of ~100 with respect to the theoretical value of a/N^2 calculated by Brussard[11] from the theory of inverse Bremsstrahlung absorption, where both free-free and free-bound collisions are kept in view. The contribution attributable to electron-neutral collisions is negligible. The

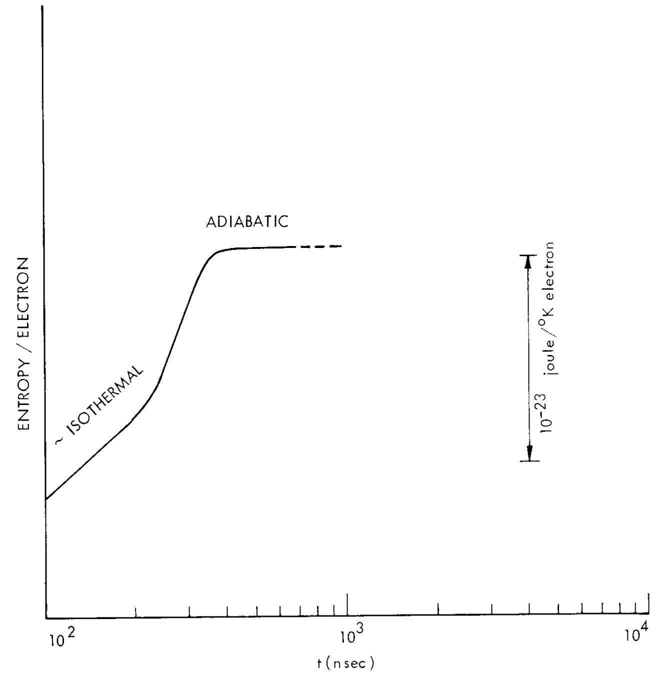

Fig. XI-37. Entropy per electron.

Brussard approximated formula gives

$$\frac{a}{N^2} = 2.31 \times 10^{-38}\, y^{1/2}(e^y-1)\, G_{ff}(\text{cm}^5), \tag{28}$$

where $y = \frac{\hbar\omega}{kT} = \frac{2.247 \times 10^4}{T}$, for the HeNe laser frequency, and G_{ff} is the Gaunt factor for free-free collision. A density profile like $N = N_o\left[1-\left(\frac{r}{R}\right)^2\right]^3$ would give a peak-average ratio of 8 which is fairly satisfying. More experimental data are needed to justify such a profile-shape analysis. A more detailed study of the plasma transmission should be done for this purpose.

From knowledge of the volume of the plasma, it is possible to know the energy that is spent by the plasma in expanding against the gas and in emitting the shock wave, just by multiplying the volume of the plasma by the external unperturbed gas pressure. For time up to 200 nsec the work is given by

$$L = 1.1 \times 10^{11}\, t^{1.8} \text{ Joules (t sec).} \tag{29}$$

The corresponding power is immediately calculated by deriving the energy. A peak value of 6×10^5 watts is found at 200 nsec.

6. Initial Temperature Estimate

Starting from the volume of the plasma at very short times, when the giant pulse is still on, and when total ionization is supposed to be achieved, we can calculate the initial electron temperature. From the initial length of the plasma (4.5 mm) and the initial diameter, $D = f\theta$, where f is the focal length of the lens (f = 68 mm), and θ is the divergence of the ruby beam (f mrad), we get $D = 3.4 \times 10^{-2}$ cm, and $V_{\text{initial}} = 4.1 \times 10^{-4}\text{cm}^3$. Supposing reasonably total ionization when the giant pulse is on, we get an initial number of electrons $N_{\text{initial}} = 10^{17}$ electrons. Knowing the ionization energy of Helium $E_{\text{ion}} = 24.58$ eV $= 3.93 \times 10^{-18}$ joule, we get immediately the energy spent in breaking down the initial crowd of atoms $E_{\text{ion initial}} = 3.9 \times 10^{-1}$ joules $\approx 4 \times 10^{-1}$ joules. Assuming that, of the 2.5 joules emitted by the laser, approximately 10% is reflected back by the entry window, we find available immediately after the breakdown approximately 1.8 joules. Extrapolating the volume curve, we find the initial volume $V = 4.1 \times 10^{-1}$ cm^3 at a time of ~10 nsec. In doing a pessimistic calculation of the temperature, we keep in mind that at 10 nsec after breakdown ~25% of the energy from the ruby has been emitted. Then the energy available for heating the plasma at a time of ~10 nsec is 0.45 joule. The absorption coefficient measured at 6328 Å is not very far away from the absorption coefficient for the ruby light at 6943 Å; at 100 nsec the measured absorption coefficient at 6328 Å is ~6 cm^{-1}. Assuming this value also for shorter time and using as a value for the length of the plasma the initial length 4.5 mm, we get an optical longitudinal thickness of 2.7. The absorbed fraction of the initial ruby energy is then, at least, $1 - e^{-2.7} = 93\%$, and so the initial crowd of electrons and ions has a total thermal energy of ~0.4 joule. The corresponding temperature is immediately found. Assuming thermal equilibrium between ions and electrons, we have

$$E = \frac{0.4}{2 \times 10^{17}} = 2 \times 10^{-18} \text{ joule/electron.}$$

Since $E = 3/2\ kT$, we find $T = 9.6 \times 10^4 \approx 10^5$ °K corresponding to 12.4 eV. The radiation loss and the extremely fast expansion cause a very fast drop of the temperature before 100 nsec. The experiment cannot give information on the temperature before 130 nsec, because of the impossibility of measuring the absorption coefficient for shorter times. In doing this measurement the experimenter should use a powerful gas laser (power of the order of 10-50 mW), so that, by bringing the lens G closer to the plasma, a larger solid angle of scattered gas-laser light could be detected by the diaphragm H; in this way, a larger emission power would be received by H. This fact would necessitate having a very powerful gas laser, since the signal must be attenuated in order not to saturate the photomultiplier tube. A weak gas-laser signal would be lost in the noise.

G. Lampis

References

1. G. Lampis, Quarterly Progress Report No. 81, Research Laboratory of Electronics, M.I.T., April 15, 1966, pp. 58-61.
2. G. Lampis, Quarterly Progress Report No. 83, Research Laboratory of Electronics, M.I.T., October 15, 1966, pp. 41-52.
3. Ibid., see Fig. VII-4, p. 45.
4. Ibid., see Fig. VII-8, p. 48, and Fig. VII-12, p. 52.
5. S. A. Ramsden and P. Savic, Nature, p. 1217, September 1964.
6. Yu. P. Raizer, Soviet Phys. – JETP 21, 1009 (1965).
7. G. V. Ostrovskaya, Yu. I. Ostrovskii, JETP Letters 4, No. 4 (1966).
8. G. A. Askar'yam, M. S. Rabinovich, et al., Soviet Phys. – JETP 1, 162 (1965).
9. M. M. Litvak and D. F. Edwards, "Electron Recombination in Laser Produced Hydrogen Plasma," Lincoln Laboratory, M.I.T., 1965.
10. C. Kittel, Elementary Statistical Physics (John Wiley and Sons, Inc., New York, 1965), p. 35.
11. P. J. Brussard and H. C. van de Hulst, Rev. Modern Phys. 34, 507 (1962).

G. MICROWAVE EMISSION FROM n-TYPE INDIUM ANTIMONIDE AT 422°K AND 77°K[*]

Larrabee[1] and Hicinbothem[2] were the first to observe microwave emission from n-type InSb when a sample was subjected simultaneously to DC magnetic and electric fields. The threshold values of B and E for onset of the emission were approximately 3000 Gauss and 200 V/cm, respectively. At these high electric fields, electron-hole avalanche occurs, and Steele[3] attributes the microwave emission to photoconductive mixing of band-gap radiation associated with this avalanche breakdown.

Buchsbaum, Chynoweth, and Feldmann,[4] and others,[5-7] have found another regime of microwave emission at relatively low electric fields ($E \approx 10$ V/cm), well below values of E required for avalanche breakdown, where the sample exhibits nearly linear current-voltage characteristics. This report is concerned exclusively with this low-field regime.

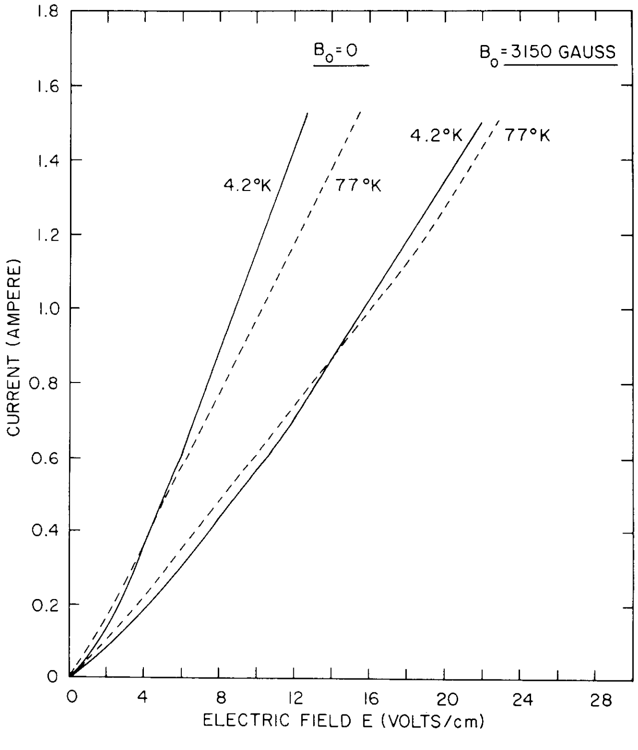

Fig. XI-38. Voltage-current characteristics of a sample of InSb.

Figure XI-38 illustrates the current-voltage characteristics as measured at 77°K and 4.2°K for the range of parameters in which studies of the microwave emission were

---

[*] This work was supported in part by the Joint Services Electronics Programs (U.S. Army, U.S. Navy, and U.S. Air Force) under Contract DA 28-043-AMC-02536(E).

made. In this, as in all succeeding experiments, the static magnetic field was parallel to the electric field.

The specific instability that gives rise to the microwave emission at low DC electric fields is not known. It has been suggested[8,9] that the instability arises from phonons that are excited by the drifting electrons. The unstable longitudinal wave then couples to an electromagnetic wave at the boundary of the sample. If this is indeed the mechanism, the phonon lifetime plays a crucial role in the determination of the threshold magnetic and electric fields for onset of instability. Theory[8,9] indicates that the threshold in electric field requires that the electron drift velocity exceed the sound velocity, while the threshold in magnetic field decreases as the phonon lifetime increases. Since the phonon lifetime at 4.2°K is much longer[10] than at 77°K, the microwave emission at 4.2°K (if, in fact, it exists at this temperature) should set in at a lower value of B. To see this change in threshold was one of the motivations for the experiments described here.

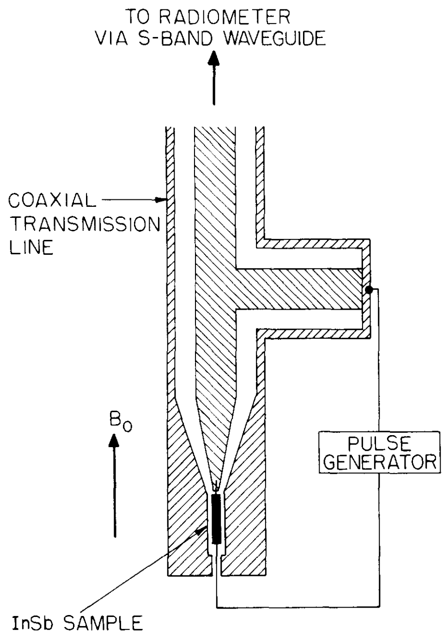

Fig. XI-39. Experimental arrangement used in the measurements of microwave noise.

A bar of InSb, $1 \times 1 \times 10$ mm^3, cut along the (110) crystal axis, was mounted near a shorted coaxial transmission line as shown in Fig. XI-39. All samples were cut from one block. For our block, the Hall mobility at 77°K and 4.2°K was in the range 2-5 $\times 10^5$ cm^2 Volts^{-1} sec^{-1}, and the carrier concentration was in the range 1-2 $\times 10^{14}$ cm^{-3}. The surface of the sample was lapped and then etched in a Bromine-Ethanol solution. The coaxial line was tapered to allow for better RF impedance matching between the sample and a standard 50-ohm line. The entire assembly was immersed in liquid nitrogen or liquid helium kept at a constant level. The sample was bathed continuoulsy by the coolant and good circulation of the liquid was insured by a number of holes drilled in the coaxial line. The axis of the sample and the DC current flow were parallel to the static magnetic field (with uncertainties in angle of less than ±2° of arc) in all the experiments reported here. The magnetic field was uniform to better than 0.5 per cent over the volume of the sample. Current pulses of 2.5-μsec duration were applied to the sample (at a repetition rate of 200 pulses/sec) through indium soldered contacts. Tin solder was also used with no observable changes in the voltage-current or microwave emission characteristics. It was also ascertained that no changes occurred when the pulse length was increased from 2.5 μsec to 7 μsec, thereby indicating that no significant heating of the crystal occurred.

The microwave signal was led through the coaxial transmission line, past a double-stub tuner and S-band waveguide to a time-resolved radiometer[11] that operated at a fixed frequency of 3000 Mc/sec, with an IF bandwidth of 10 Mc/sec. The IF amplifier was gated with a 2-μsec gate so that the noise emission was received only during the central portion of the 2.5-μsec current pulse. The noise power from the sample was compared repetitively with the noise power emitted by a standard noise source that had an equivalent noise temperature of 18,500°K. Thus the absolute noise power from the sample could be measured.

Figure XI-40 is a plot of the threshold magnetic field as a function of the threshold electric field for measurements on a given sample at 4.2°K and 77°K. Threshold is defined as that value of B and E for which the emitted noise power had an equivalent temperature of 100°K. This value of temperature is near the limit of sensitivity of our radiometer. The results shown for 77°K agree qualitatively with observations of Musha et al.[5] We see from Fig. XI-40 that the threshold magnetic field for onset of

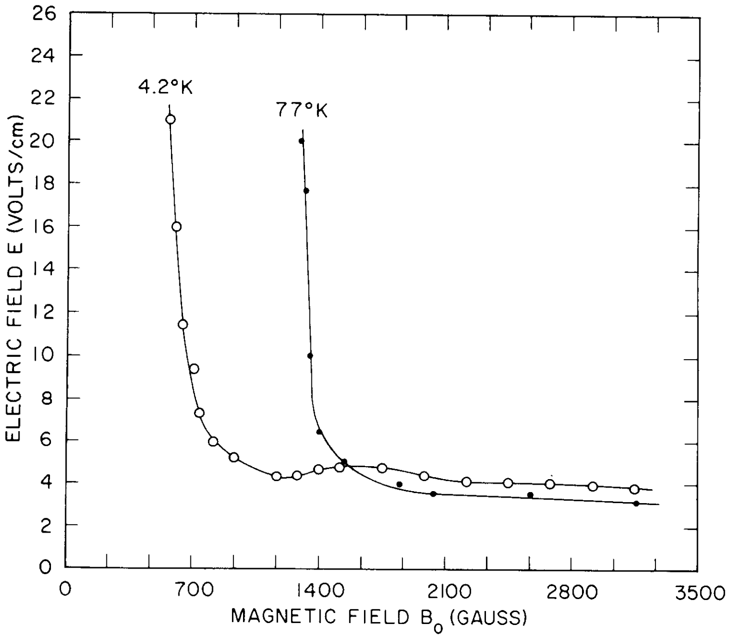

Fig. XI-40. Threshold electric field vs threshold magnetic field. Emission occurs above and to the right of a given line.

emission at 4.2°K is approximately half that at 77°K.

The dependence of the radiation intensity on magnetic field (above threshold) is illustrated in Fig. XI-41 for different values of electric field. These measurements made at 77°K are qualitatively the same as those obtained by Buchsbaum et al.[4] Figure XI-42 shows how the emitted intensity varies with electric field at constant magnetic field. This and the previous figure exhibit clearly the sharp threshold values of E and B. Data such as these were used in plotting the threshold curves of Fig. XI-40.

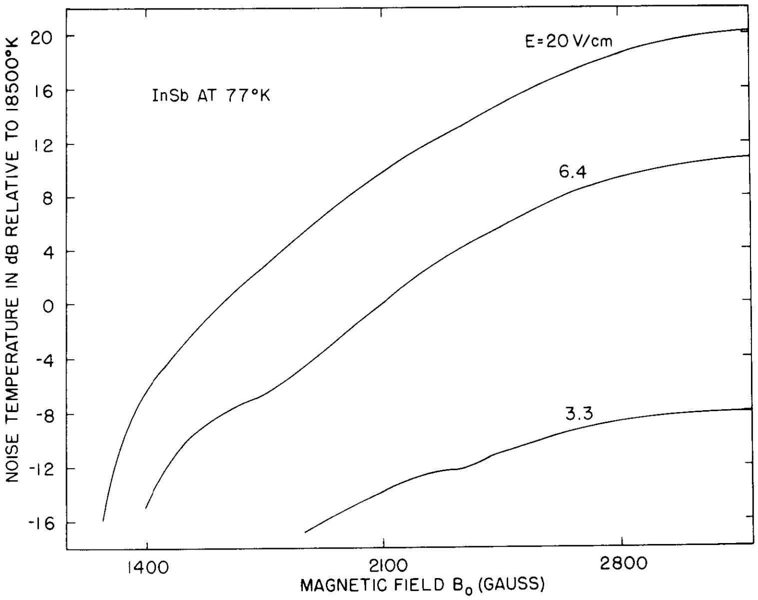

Fig. XI-41. Noise-power output as a function of magnetic field for various values of applied electric field, at 77°K.

Measurements of the emission as a function of magnetic field made at 4.2°K differ quite dramatically from those shown in Fig. XI-41. We now see in Fig. XI-43 that superposed on the monotonically increasing background emission are resonant spikes. Such spikes do not occur at 77°K.

We have labeled the spikes with a series of integers n from 1 to 11. As the electric field on the sample is decreased, a given spike moves to higher values of magnetic field. This increase in B is very nearly the same as the corresponding increase in the threshold value of B shown in Fig. XI-40 for the monotonic "continuum" radiation. Indeed, at some values of E, the first spike occurs precisely at the threshold of the "continuum" radiation (see spike n = 1 of Fig. XI-43). These observations suggest that the "spikey" and "continuum" emission processes are coupled to one another.

A given spike n is sometimes not excited or it is too small to be resolved. This is

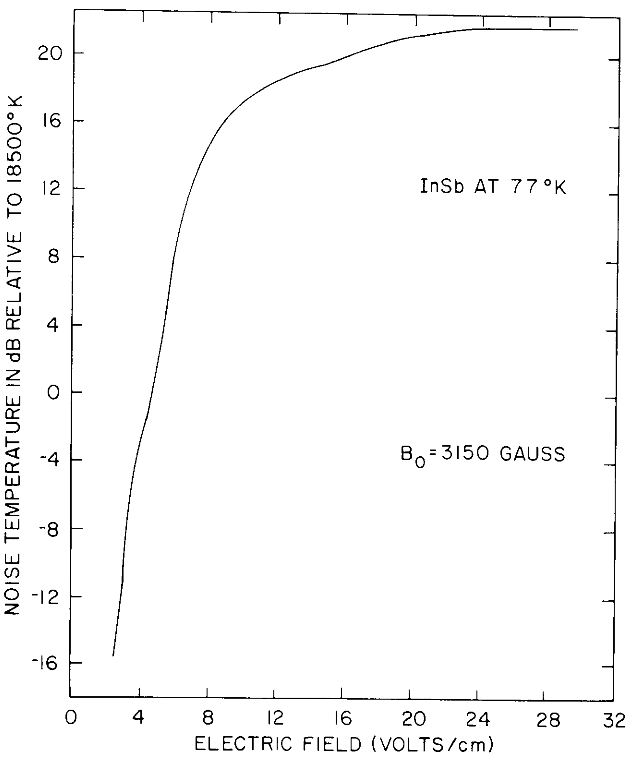

Fig. XI-42. Noise power as a function of electric field measured at 77°K.

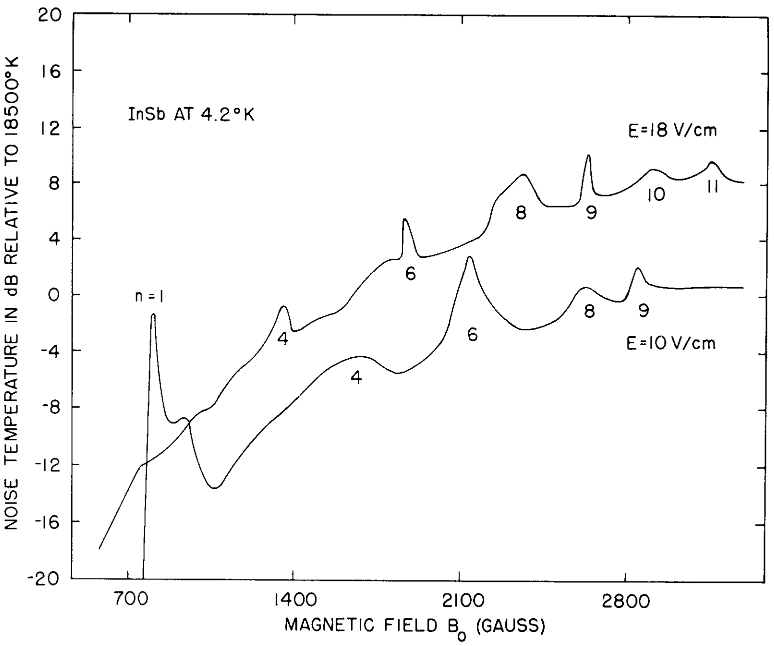

Fig. XI-43. Noise-power output as a function of magnetic field, as measured at 4.2°K. (This figure should be compared with Fig. XI-41.)

indicated in Fig. XI-43. For example, for E = 18 V/cm, spikes 1, 2, 3, 5, 7 are missing. If we accept this possibility of missing spikes, we are led to the conclusion that the spikes are nearly equally spaced with a spacing of approximately 255 Gauss. This fact is confirmed in Fig. XI-44 where the magnetic field value of a given spike n is plotted as a function of n.

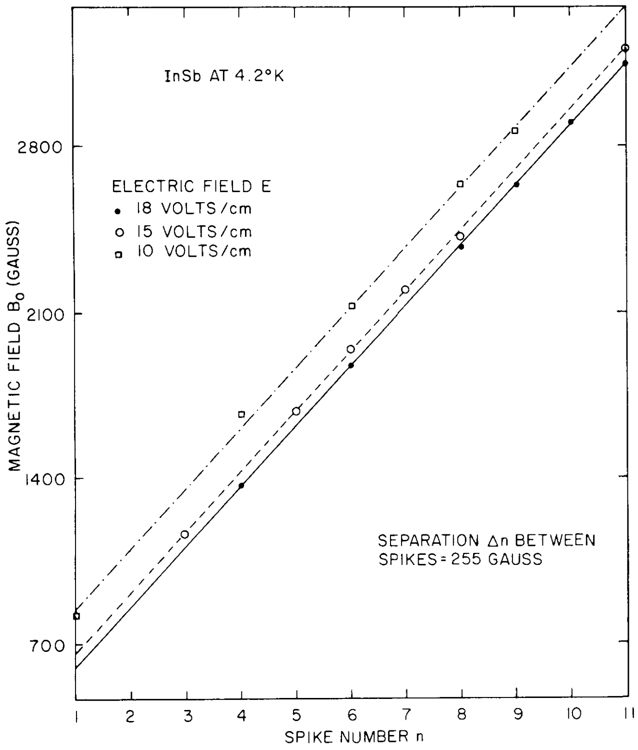

Fig. XI-44.

Position in magnetic field of a given spike, n, as a function of n. The labeling of the spikes is as shown in Fig. XI-43. Note that whether or not a spike is missing appears to be a random event.

All of the observations above refer to measurements made on a single sample of InSb and for one polarity of the applied electric field. When the polarity was reversed the only significant change was in the over-all power level of the continuum radiation. Changes as high as 5 db were noted. Different samples exhibited variations of power level by as much as 10 db. The separation between spikes from sample to sample varied, however, less than 5 per cent.

G. Bekefi, A. Bers

References

1. R. D. Larrabee, Bull. Am. Phys. Soc. 9, 258 (1964).
2. R. D. Larrabee and W. A. Hicinbothem, Proc. Symposium on Plasma Effects in Solids, Paris, 1964, Vol. 2, p. 181.
3. M. C. Steele, RCA Review 27, 263 (1966).

4. J. Buchsbaum, A. G. Chynoweth, and W. L. Feldmann, Appl. Phys. Letters 6, 67 (1965).
5. T. Musha, F. Lindvall, and J. Hagglund, Appl. Phys. Letters 8, 157 (1966).
6. D. K. Ferry, R. W. Yound, and A. A. Dougal, J. Appl. Phys. 36, 3684 (1965).
7. J. C. Eidson and G. S. Kino, Appl. Phys. Letters 8, 183 (1966).
8. A. Bers and T. Musha, Quarterly Progress Report No. 79, Research Laboratory of Electronics, M. I. T., October 15, 1965, pp. 99-109.
9. T. Musha and A. Bers, Bull. Am. Phys. Soc. 11, 569 (1966).
10. K. W. Nill, Ph. D. Thesis, Department of Electrical Engineering, M. I. T., May 1966; Proc. Int. Conf. Phys. of Semiconductors, Kyoto, Japan, 1966, p. 755.
11. G. Bekefi, Radiation Processes in Plasmas (John Wiley and Sons, Inc., New York, 1966), p. 334.
12. S. R. J. Brueck and A. Bers, Quarterly Progress Report No. 83, Research Laboratory of Electronics, M. I. T., October 15, 1966, pp. 72-76.